

Observations of nonlinear momentum fluxes over the inner continental shelf

Thomas P. Connolly¹ and Steven J. Lentz²

¹Moss Landing Marine Laboratories

San José State University

8272 Moss Landing Rd., Moss Landing, CA, 95039

tconnolly@mlml.calstate.edu (corresponding author)

²Woods Hole Oceanographic Institution

266 Woods Hole Road, MS 21, Woods Hole, MA, 02543

slentz@whoi.edu

June 21, 2021

This is a preprint of a peer-reviewed manuscript which has been accepted for publication at the Journal of Marine Research. When available, a link to the published version of this manuscript will be available via the “Peer-reviewed Publication DOI” link on EarthArXiv.

Preprint DOI: <https://doi.org/10.31223/X5531C>

ABSTRACT

1
2 Nonlinear momentum fluxes over the inner continental shelf are examined using moored
3 observations from multiple years at two different locations in the Middle Atlantic Bight.
4 Inner shelf dynamics are often described in terms of a linear alongshore momentum bal-
5 ance, dominated by frictional stresses generated at the surface and bottom. In this study,
6 observations over the North Carolina inner shelf show that the divergence of the cross-
7 shelf flux of alongshore momentum is often substantial relative to the wind stress during
8 periods of strong stratification. During upwelling at this location, offshore fluxes of along-
9 shore momentum in the surface layer partially balance the wind stress and reduce the role
10 of the bottom stress. During downwelling, onshore fluxes of alongshore momentum re-
11 inforce the wind stress and increase the role of bottom stress. Over the New England
12 inner shelf, nonlinear terms have less of an impact in the momentum balance and exhibit
13 different relationships with the wind forcing. Differences between locations and time pe-
14 riods are explained by variations in bottom slope, latitude, vertical shear and cross-shelf
15 exchange. Over the New England inner shelf, where moored density data are available,
16 variations in vertical shear are explained by a combination of thermal wind balance and
17 wind stress. An implication of this study is that cross-shelf winds can potentially influence
18 the alongshore momentum balance over the inner shelf, in contrast with deeper locations
19 over the middle to outer shelf.

20 **Keywords**— Momentum balance, Nonlinear, Momentum flux, Coastal dynamics, Upwelling
21 dynamics, Downwelling dynamics, Thermal wind balance, Inner shelf

22 **1. Introduction**

23 The dynamics of the inner continental shelf govern exchange between shallower wa-
24 ters in the surf zone and deeper waters over the middle to outer shelf. The inner shelf
25 is often dynamically defined as a region where the surface and bottom boundary layers
26 interact and turbulent stresses are present throughout the entire water column (Mitchum
27 and Clarke, 1986; Lentz, 1995; Lentz and Fewings, 2012). The inner shelf region is also
28 characterized by cross-shelf mass transport that is reduced from the theoretical Ekman
29 transport expected for deeper water (Lentz et al., 1999; Kirincich et al., 2005). The off-
30 shore extent of the inner shelf is strongly influenced by stratification, which inhibits tur-
31 bulent mixing and restricts the region of reduced cross-shelf transport to shallower depths
32 (Lentz et al., 1999). Unlike the middle to outer shelf, cross-shelf winds often drive signifi-
33 cant transport and influence turbulent mixing over the inner shelf (Tilburg, 2003; Fewings
34 et al., 2008; Horwitz and Lentz, 2014). In the unique dynamical regime of the inner shelf,
35 cross-shelf exchange is part of a complex set of interactions between wind forcing, strati-
36 fication, density fronts and boundary-layer turbulence.

37 The alongshore momentum balance is frequently used as a framework for understand-
38 ing the dynamics of coastal regions, including the inner shelf. The depth-averaged balance
39 over the inner shelf is often characterized as being dominated by the frictional terms, wind
40 stress and bottom stress, with secondary contributions from local acceleration and along-
41 shore pressure gradients (Hickey, 1989; Lentz et al., 1999; Lentz and Fewings, 2012). The
42 alongshore pressure gradient has also been shown to be important in balancing the wind
43 stress at some locations, particularly at locations near alongshore variations in bathymetry
44 and coastline (Kirincich and Barth, 2009b; Fewings and Lentz, 2010). However, the po-
45 tential impact of additional nonlinear terms in the alongshore momentum balance is not
46 well known and is often neglected for simplicity (Lentz and Fewings, 2012). If nonlinear
47 terms are significant, neglecting them could lead to misinterpretation of the magnitude of
48 stresses at the bottom or in the interior of the water column, which are often uncertain

49 or unknown. The goal of this study is to assess the importance of nonlinear momentum
50 fluxes in observations at different locations, and provide a mechanistic understanding of
51 how they arise in response to wind forcing over the inner shelf.

52 In deeper water over the middle to outer shelf, nonlinear momentum fluxes have
53 been found to strongly influence upwelling dynamics under certain conditions. Lentz
54 and Chapman (2004) show that the divergence of the cross-shelf flux of alongshore mo-
55 mentum is important in balancing upwelling-favorable alongshore wind stress over conti-
56 nental shelves characterized by strong stratification and a steep bottom slope. At locations
57 with strong stratification and steep bottom slope, the role of bottom friction is reduced
58 and the onshore return flow occurs in the geostrophic interior region between the turbu-
59 lent boundary layers, rather than in the bottom boundary layer. Theory also predicts that
60 cross-shelf momentum flux divergence reinforces the wind stress during downwelling-
61 favorable wind forcing, allowing the magnitude of the bottom stress to exceed that of the
62 wind stress (Lentz and Chapman, 2004). The role of the nonlinear momentum flux di-
63 vergence is unclear over the inner shelf where the boundary layers interact, there is no
64 distinct geostrophic interior region and cross-shore wind stress can be an important part
65 of the forcing.

66 Previous studies that have taken nonlinear terms into account over the inner shelf have
67 focused on a range of different mechanisms and have reached different conclusions about
68 the importance of nonlinear processes. In Monterey Bay on the central California coast,
69 Woodson (2013) found that nonlinear interaction between offshore surface transport and
70 relative vorticity associated with the alongshore flow can be important in balancing wind
71 stress in the surface layer, along with the Coriolis force. These observations, combined
72 with high levels of stratification and shallow estimates of the boundary layer thickness,
73 suggest that the reduction of surface transport from theoretical Ekman transport is not
74 necessarily associated with significant stress at the base of the surface layer. Over the Ore-
75 gon inner shelf, Kirincich and Barth (2009b) found the divergence of the cross-shelf flux

76 of along-shelf momentum to be important in balancing the wind stress. The presence of
77 strong vertical shear in these observations indicates that the mechanism is similar to that
78 described by Lentz and Chapman (2004) for mid-shelf locations, although the importance
79 of the nonlinear term over the Oregon inner shelf varies at different sites along the same
80 isobath with similar stratification and bottom slope. Estimates of this nonlinear term are
81 also substantial relative to the wind stress during periods of strong stratification over the
82 Catalan inner shelf in the Mediterranean (Grifoll et al., 2012). However, numerical mod-
83 eling over the West Florida shelf indicates that the nonlinear terms are small, consistent
84 with a linear balance (Liu and Weisberg, 2005). Observations from a range of different
85 locations, and subject to a range of different forcing conditions, are needed to clarify the
86 role of this nonlinear process over the inner shelf.

87 This study assesses the role of nonlinear momentum fluxes in the alongshore mo-
88 mentum balance at two different inner shelf locations in the Middle Atlantic Bight: the
89 Martha's Vineyard Coastal Observatory (MVCO) over the New England inner shelf and
90 the Army Corps of Engineers Field Research Facility (FRF) over the North Carolina inner
91 shelf (Fig. 1). Because of differences in latitude and coastline orientation, these two loca-
92 tions are subject to different seasonal variations in wind forcing, but a strong cross-shelf
93 component of wind stress is present at both locations (Lentz, 2008a). Tidal height ampli-
94 tudes at the dominant M2 frequency are between 0.4–0.5 m at each site, but tidal current
95 amplitudes increase substantially from <0.1 m/s near FRF from ~ 0.3 m/s near MVCO
96 (Moody et al., 1984). At MVCO, the alongshore momentum balance has primarily been
97 examined in a linearized framework, and a dominant balance between the wind stress and
98 alongshore pressure gradient has been observed (Fewings and Lentz, 2010). At FRF, Lentz
99 et al. (1999) also examined a linearized momentum balance and identified a dominant bal-
100 ance between the wind stress and bottom stress. Nonlinear terms have also been neglected
101 in the alongshore momentum balance integrated over the surface layer at this site (Lentz,
102 2001). However, numerical modeling suggests that nonlinear momentum fluxes strongly

103 influence the alongshore momentum balance at FRF, playing a major role in balancing the
104 wind stress during upwelling and a more minor role in reinforcing the wind stress during
105 downwelling (Kuebel Cervantes et al., 2003; 2004). In the present study, observations
106 from both sites are compared under a range of forcing conditions to assess the importance
107 of the nonlinear terms and identify physical mechanisms that determine how and when
108 they become important.

109 At each location, data from long-term current meter arrays are used to evaluate the
110 importance of the nonlinear terms in alongshore momentum balances. In Section 2, along-
111 shore momentum balance equations are presented in two forms, both depth-averaged and
112 integrated over the surface layer. Observations and methods for estimating terms of the
113 momentum balance are presented in Section 3. Descriptive overviews of the MVCO and
114 FRF observations are provided (Section 4.a), before presenting analyses of the depth-
115 averaged and surface-integrated momentum balances (Sections 4.b,c). Processes influenc-
116 ing vertical shear, an important component of the nonlinear momentum flux divergence,
117 are evaluated using moored density time series observations at MVCO (Section 4.d). As
118 discussed in Section 5, it is found that the contrasting patterns of wind forcing and cross-
119 shelf exchange at MVCO and FRF lead to different relationships between the alongshore
120 wind stress and the momentum flux divergence. These differences can be explained by
121 a combination of bottom slope, vertical shear, the Coriolis parameter, and the fraction of
122 cross-shelf surface transport relative to the deep water Ekman transport.

123 **2. Alongshore momentum balances**

124 To provide a theoretical framework for the analysis, simplified alongshore momen-
125 tum balances are developed for the inner continental shelf. The primary purpose of the
126 momentum balance analysis is to assess the importance of the cross-shelf momentum flux
127 divergence. A major simplification is the assumption of a two-dimensional mass balance,
128 neglecting alongshore variations in currents and the surface gravity wave field. There is

129 evidence for this type of mass balance at both inner-shelf locations examined in this study
130 when the effects of wave-driven transport are included (Lentz et al., 2008). However, this
131 assumption would not be valid in locations where alongshore variations in topography
132 are present over short scales and alongshore advection of momentum can be important
133 in balancing localized pressure gradients (e.g. Ofsthun et al., 2019). The effects of wave
134 breaking in the surf zone are also not included in the analysis, which focuses on the inner
135 shelf region offshore of the surf zone.

136 The effects of unbroken surface gravity waves over the inner shelf are accounted for
137 by considering the wave-averaged Lagrangian cross-shelf velocity $\mathbf{u}_L = \mathbf{u} + \mathbf{u}_{st}$, where
138 \mathbf{u} is the wave-averaged Eulerian velocity vector and \mathbf{u}_{st} is the Stokes drift vector. Wave-
139 averaged observations collected by a current meter at a fixed location represent only the
140 Eulerian component \mathbf{u} , but \mathbf{u}_{st} also contributes to additional transport of mass and trac-
141 ers in the direction of wave propagation (Monismith and Fong, 2004). The presence of
142 the Stokes drift, \mathbf{u}_{st} , influences the alongshore momentum balance through the Stokes-
143 Coriolis force (Xu and Bowen, 1994; Lentz et al., 2008) and vortex force terms (Smith,
144 2006; Uchiyama et al., 2010).

145 *a. Depth-averaged momentum balance*

146 As a starting point for developing a simplified two-dimensional momentum balance
147 for the inner shelf, a three-dimensional balance that includes the effects of wave breaking
148 is first considered. The x coordinate is defined as positive offshore, and the y coordinate
149 is oriented alongshore (Fig. 1b,c). Following Uchiyama et al. (2010), a depth-averaged
150 alongshore momentum balance that includes the effects of both breaking and unbroken
151 surface waves can be written in a flux-divergence form,

$$\begin{aligned} \frac{\partial \bar{v}}{\partial t} + \frac{1}{D} \frac{\partial}{\partial x} \int_{-h}^{\eta} (u_L v) dz + \frac{1}{D} \frac{\partial}{\partial y} \int_{-h}^{\eta} (v_L v) dz - \left(\overline{u_{st} \frac{\partial u}{\partial y}} \right) - \left(\overline{v_{st} \frac{\partial v}{\partial y}} \right) \\ = -\frac{1}{\rho_o} \frac{\partial \bar{p}}{\partial y} - f \bar{u}_L + \frac{\tau^{sy}}{\rho_o D} - \frac{\tau^{by}}{\rho_o D} + \frac{\epsilon k^y}{\rho_o D \sigma} \end{aligned} \quad (1)$$

152 where η is sea level, h is bottom depth, $D = \eta + h$ is the total thickness of the water
 153 column, $\rho_o = 1025 \text{ kg/m}^3$ is a constant reference density, f is the Coriolis parameter,
 154 τ^{sy} is the alongshore component of surface wind stress, τ^{by} is the alongshore component
 155 of bottom stress, ϵ is the wave dissipation rate, k^y is the alongshore component of the
 156 wavenumber, and σ is the wave frequency. Overbars indicate depth-averaged quantities,
 157 for example,

$$\bar{v} = \frac{1}{D} \int_{-h}^{\eta} v dz. \quad (2)$$

158 Assuming a two-dimensional mass balance ($\bar{u}_L = 0$), neglecting the effects of wave
 159 dissipation outside of the surf zone, and neglecting alongshore variations in currents and
 160 waves, the alongshore momentum balance in equation (1) can be simplified as

$$\frac{\partial \bar{v}}{\partial t} + \frac{1}{D} \frac{\partial}{\partial x} \int_{-h}^{\eta} (u_L v) dz = -\frac{1}{\rho_o} \frac{\partial \bar{p}}{\partial y} + \frac{\tau^{sy}}{\rho_o D} - \frac{\tau^{by}}{\rho_o D}. \quad (3)$$

161 The left-hand side of equation (3) includes local acceleration and the nonlinear momen-
 162 tum flux divergence term. This nonlinear term could be decomposed into 1) nonlinear
 163 advection of alongshore momentum by the cross-shore Eulerian circulation and 2) the
 164 vortex force induced by the interaction of the cross-shelf component of Stokes drift and
 165 the alongshore current,

$$\frac{\partial}{\partial x} \int_{-h}^{\eta} (u_L v) dz = \frac{\partial}{\partial x} \int_{-h}^{\eta} (uv) dz + \frac{\partial}{\partial x} \int_{-h}^{\eta} (u_{st} v) dz \quad (4)$$

166 Including transport due to Stokes drift is important because it often exceeds the wind-

167 driven transport in the surface layer at locations inshore of the 20-m isobath at MVCO and
 168 FRF (Lentz et al., 2008). Over the Martha’s Vineyard inner shelf, 15-30% of the cross-
 169 shelf heat flux during summer is associated with Stokes drift (Fewings and Lentz, 2011).
 170 However, Stokes drift is only one component of the wave-driven circulation. The Stokes-
 171 Coriolis force induces an Eulerian wave-driven flow which tends to cancel the Stokes drift
 172 in the limit of weak eddy viscosity (Xu and Bowen, 1994; Lentz et al., 2008). To assess the
 173 net impact of Stokes drift and Eulerian advection, these two components are combined into
 174 a single nonlinear momentum flux divergence term. This term is potentially significant if
 175 there is net cross-shelf exchange due to wind and waves ($u_L \neq 0$), vertical shear in the
 176 alongshore current is present ($\partial v/\partial z \neq 0$), and cross-shelf variations exist ($\partial/\partial x \neq 0$).
 177 This nonlinear term is present in a simplified two-dimensional framework, but it is not
 178 present in one-dimensional models of the water column.

179 The present study primarily uses information from cross-shelf current meter arrays
 180 deployed over multiple years at two different inner shelf locations. Although data are
 181 not available to accurately estimate the alongshore pressure gradient term, the current
 182 meter data allow for estimates of the nonlinear term. Estimates of the nonlinear term
 183 are compared with estimates of surface and bottom stresses, and the importance of the
 184 nonlinear term is assessed under different wind forcing and stratification conditions.

185 *b. Surface layer momentum balance*

186 The alongshore momentum balance is also analyzed over a portion of the water col-
 187 umn near the surface in order to relate the nonlinear dynamics to cross-shelf exchange and
 188 turbulent stresses. Cross-shore surface transport U_S is calculated from the vertical integral
 189 of the Lagrangian cross-shelf velocity in the upper layer of the water column

$$U_S = \int_{z_s}^{\eta} u_L dz, \quad (5)$$

190 where z_s is the depth of the first zero crossing in the vertical profile of u_L . The terms in
 191 the alongshore momentum balance are integrated over this same surface layer.

192 Consistent with the depth-averaged balance described above in Section 2.a, the sur-
 193 face layer momentum balance considered in this study neglects alongshore variations in
 194 currents and waves, as well as wave dissipation in the surf zone. The alongshore momen-
 195 tum balance integrated over the upper layer is given by

$$\frac{\partial}{\partial t} \int_{z_s}^{\eta} v dz + \frac{\partial}{\partial x} \int_{z_s}^{\eta} (u_L v) dz - (w_L v)|_{z=z_s} = -\frac{1}{\rho_o} \int_{z_s}^{\eta} \frac{\partial p}{\partial y} dz - fU_s + \frac{\tau^{sy}}{\rho_o} - \frac{\tau^{iy}}{\rho_o} \Big|_{z=z_s} \quad (6)$$

196 where w_L is the Lagrangian vertical velocity and $\tau^{iy}|_{z=z_s}$ is the interior turbulent stress at
 197 the base of the surface layer. The Lagrangian vertical velocity at the base of the surface
 198 layer can be determined from conservation of volume,

$$w_L|_{z=z_s} = \frac{\partial \eta}{\partial t} + \frac{\partial U_s}{\partial x}. \quad (7)$$

199 Like the depth-averaged momentum balance, the left hand side of the surface layer
 200 momentum balance in equation (6) contains a local acceleration term in addition to non-
 201 linear terms. The two nonlinear terms represent the net flux of alongshore momentum into
 202 the surface layer at a given cross-shelf location. Both the cross-shore and vertical compo-
 203 nents of the Lagrangian velocity \mathbf{u}_L contribute to the flux of alongshore momentum into
 204 the surface layer. Both of these terms are dependent on cross-shore variations ($\partial/\partial x$) and
 205 cannot exist in one-dimensional models of the water column, even those with sophisti-
 206 cated turbulence closure schemes. Although direct observations of interior stresses are not
 207 available in this study, implications of the results for turbulent stresses over the inner shelf
 208 will be discussed.

209 **3. Methods**

210 *a. Data sources*

211 To address the role of nonlinear terms in the momentum balance, this study uses
212 observations from Duck, NC, and Martha’s Vineyard, MA (Fig. 1). At both of these sites,
213 velocity data are available for several years at multiple cross-shelf locations.

214 *i. Duck, NC* A long-term array of five acoustic current profilers at bottom depths of
215 5-11 m, was maintained by the Army Corps of Engineers Field Research Facility (FRF)
216 at Duck, North Carolina (Fig. 1b). Velocity data from the time period November 2008 to
217 July 2014 are used in this study. These data are publicly available on the FRF data portal.
218 At the 5, 6, 8 and 11m sites, Nortek Acoustic Wave and Current (AWAC) profilers obtain
219 velocity profiles with vertical resolution of 0.5 m. The bottom velocity bins are located
220 1.5m above the bottom at the 5 and 6m sites and 1.0m above the bottom at the 8 and 11m
221 sites. Data from bins within 2 m of the mean sea surface are not included in the analysis.
222 The AWAC profilers also obtain measurements of surface gravity wave characteristics,
223 including significant wave height (H_{sig}), peak period and direction.

224 Stokes drift profiles, \mathbf{u}_{st} , and depth averages, $\bar{\mathbf{u}}_{st}$, are computed from observed bulk
225 wave characteristics (H_{sig} , peak period, direction) following Lentz et al. (2008). Time pe-
226 riods when sites are in the surf zone are excluded from the analysis based on a conservative
227 criterion of $H_{sig} < 0.33h$. When wave data are not available at a site, wave height and
228 period from the nearest available site are used and direction is calculated from the nearest
229 available site using Snell’s law. Remaining short gaps of up to 6 hours in \mathbf{u}_{st} and $\bar{\mathbf{u}}_{st}$ are
230 filled using linear interpolation. Gaps of the same size in the FRF ADCP velocities are
231 filled by first removing tidal velocities, linearly interpolating over the gaps, then adding
232 back the tidal velocities. The tidal analysis is performed using a Python distribution of
233 UTide (Codiga, 2011), using tidal constituents with periods of less than 48 hours. At each
234 site, all current and Stokes drift vectors are rotated so that the y axis is aligned with princi-
235 pal axis of $\bar{\mathbf{u}}_L$. The principal axis angles vary between 18.4-21.6° counter-clockwise from

236 true north.

237 In addition to the long-term current meter array, conductivity, temperature and depth
238 (CTD) profiles are collected on a nominal daily basis from the end of a pier at FRF (Fig.
239 1b). These data are used to provide information on water column stratification. Profiles of
240 water column temperature and practical salinity are available through the FRF data portal.
241 Wind speed and direction at the FRF site are measured by an anemometer at a height of
242 16.4 m above the water at the end of the FRF pier (NDBC station DUKN7). Wind vectors
243 at FRF are rotated into a coordinate system in which the y axis is 20° counter-clockwise
244 from true north.

245 Nearshore bathymetry data (Fig. 1b) near Duck, NC were collected by Dr. Jesse
246 McNinch and are available in Thielier et al. (2013). Nearshore bathymetry data used
247 for depths 2.5-9 m are gridded at 10-m horizontal resolution; data used for depths 10
248 m and greater are gridded at 40-m horizontal resolution. Regional-scale bathymetry data
249 on a 30 arc-second grid were obtained from the General Bathymetric Chart of the Oceans
250 GEBCO_2014 Grid, version 20150318 (<http://www.gebco.net>, Fig. 1a).

251 *ii. Martha's Vineyard, MA* As part of the Stratification, Wind, and Waves on the Inner
252 shelf of Martha's Vineyard (SWWIM) field program, an array of moorings was deployed
253 during the time period from October 2006 to February 2010. The cross-shelf array con-
254 sisted of four sites ranging in depth from 7 m to 27 m. A description of the complete
255 data set is given by Horwitz and Lentz (2016), and a brief summary of the relevant data is
256 provided here.

257 To facilitate comparison with the data from FRF, where the deepest site is at 11 m,
258 this study focuses on the two inshore SWWIM sites at 7 m and 12 m (Fig. 1c). Velocity
259 data from the 7-m site were obtained from an upward-looking 1200 kHz ADCP. Vertical
260 bins used for analysis span heights from 1.75 m above the bottom to within 0.75 m from
261 the surface, with 0.25 m vertical spacing. Data were collected at 1 Hz in 6.7 min or 9 min
262 bursts and averaged every 20 min. At the 12-m site, a 1200-kHz ADCP collected data at a

263 cabled node of the MVCO. Vertical bins used for analysis span heights from 2.5 m above
264 the bottom to within 2.5 m below the surface, with 0.5 m vertical spacing. Data were
265 collected at 2 Hz and averaged into 20 min ensembles. The ADCP data at the 12-m site
266 are also used to compute wave characteristics, including H_{sig} , peak period and direction.
267 Stokes drift is calculated in the same manner as the FRF data. In the SWWIM data, where
268 tidal velocities account for a greater fraction of the variance, a more restrictive threshold
269 of 1 hour is used for linear interpolation of gaps. Principal axis angles in the SWWIM data
270 are computed from $\bar{\mathbf{u}}$ during time periods when waves are relatively small ($H_{sig} < 0.75$)
271 following Lentz et al. (2008). Calculating the principal axis based on all $\bar{\mathbf{u}}_L$ data results in
272 differences of 1.2° or less depending on the site.

273 In addition to velocity, time series of seawater density and wind are used at this site.
274 Seawater density is calculated from temperature and conductivity data collected at the 7
275 m and 12 m sites using SBE-37 MicroCATs spaced at 2 m intervals throughout the water
276 column. Wind speed and direction data are obtained from the MVCO beach meteorolog-
277 ical mast, at a height 12 m above the surface. The wind data are rotated into the same
278 coordinate system defined by principal axis of the 12-m site.

279 *b. Estimates of momentum balance terms*

280 The focus of this study is assessing the importance of the nonlinear terms in the mo-
281 mentum balances in equations (3) and (6). Since the nonlinear terms contain derivatives in
282 the cross-shore direction, mooring data from two adjacent sites at different bottom depths
283 are used to estimate this term. Vertical integrals of $(u_L v)$ are estimated at the inshore
284 and offshore sites before taking their difference. The average of the two bottom depths is
285 used for D . Where sufficient data are available, estimates of additional terms are averaged
286 between the same two sites. At the FRF site, the momentum balance analysis focuses on
287 the 6 m and 8 m sites due to availability of overlapping ADCP data. At the MVCO site,
288 analysis focuses on data from the 7 m and 12 m sites.

289 Vertical integrals involving ADCP data, such as the depth integral of v in equation (2),

290 are estimated using the trapezoidal rule. Velocity is linearly interpolated from the bottom
291 bin to zero at the seabed and extended from the top bin upward to the sea surface. The
292 depth-averaged cross-shelf velocity \bar{u}_L is subtracted from the cross-shelf velocity profile
293 before estimating vertical integrals of u_L and $(u_L v)$, which enforces a two-dimensional
294 mass balance in which the net surface transport is zero. This isolates the depth-dependent
295 circulation associated with wind-driven upwelling and downwelling, and is consistent with
296 previous studies of the cross-shelf circulation at FRF and MVCO (Lentz, 2001; Fewings
297 et al., 2008). In calculating the surface transport U_s (equation 5), the depth of the first
298 zero crossing, z_s , in the vertical profile of u_L is estimated using linear interpolation. The
299 vertical component of Lagrangian velocity, w_L in equation (7), is estimated using the dif-
300 ference between U_s at the two stations. The contribution of the temporal derivative in sea
301 surface height was found to be negligible in the calculation of w_L and is neglected. To
302 estimate the vertical momentum flux term in equation (6), values of v are interpolated to
303 the zero crossing depth z_s at each station and averaged. Time derivatives of local accel-
304 eration are estimated using a center difference method. Estimates of momentum balance
305 terms are made from unfiltered (20 minute or hourly) data, then low-pass filtered to focus
306 on subtidal time scales. Low pass filtered quantities are computed using a PL64 filter with
307 a half-amplitude period of 33 hours (Rosenfeld, 1983).

308 Estimates of the nonlinear term at FRF are further restricted to time periods when the
309 assumption of two dimensional mass balance is justified. We restrict analysis of the FRF
310 data to time periods when the magnitude of the depth averaged cross-shelf velocity $|\bar{u}_L| <$
311 0.03 m/s. The magnitude of \bar{u}_L exceeds this threshold 3-8% of the time at the different
312 sites at FRF. This does not occur during June–August at the 6m or 8m sites, where much
313 of the detailed analysis is focused. Restricting the analysis to times when $|\bar{u}_L| < 0.03$
314 m/s excludes the effects of three-dimensional processes which could be important in the
315 momentum balance but cannot be evaluated with the cross-shelf mooring arrays used in
316 this study.

317 Surface and bottom stress estimates are made using bulk formulas. Wind stress is
 318 computed using the quadratic drag coefficient formulation of Smith (1988). Two different
 319 formulations are used to estimate bottom stress from the ADCP observations at the FRF
 320 site. First, a quadratic drag law is used, assuming a logarithmic boundary layer. The
 321 roughness length, z_o is estimated from $z_o = k_s/30$, where k_s is a grain roughness. The grain
 322 roughness is computed as $k_s = 2.5D$, using the median grain size $D = 0.017$ cm at Duck,
 323 NC (Lee et al., 2002). In terms of a drag coefficient $C_D = [\kappa/\ln(z/z_o)]^2$, where κ is Von
 324 Karman's constant, the resulting value of $z_o = 1.4 \times 10^{-5}$ m corresponds to $C_D = 1.3 \times 10^{-3}$
 325 at a height 1 m above the bed. The use of a constant z_o based on grain roughness neglects
 326 effects of a rippled bed, wave-current interaction and near-bed stratification. However,
 327 this value is close to the value of $C_D = 1.0 \times 10^{-3}$ obtained by Feddersen et al. (1998)
 328 from a best fit between wind stress and bottom stress seaward of the surf zone at Duck,
 329 NC. In addition to the quadratic drag law, a linear drag coefficient of 5×10^{-4} m/s is also
 330 tested for consistency with the study of Lentz et al. (1999). Since detailed measurements
 331 of the bottom boundary layer are not available to constrain bottom stress estimates in this
 332 study, these simple formulations are used for consistency with previous literature, and the
 333 implications of uncertainty in the physics will be discussed.

334 4. Results

335 a. *Description of variability over the inner shelf*

336 Basic descriptions of wind forcing, stratification and velocity are presented first to pro-
 337 vide context for the momentum balance analysis. Stratification has the potential to influ-
 338 ence nonlinear momentum fluxes by promoting the development of cross-shelf exchange
 339 and vertical shear. Density stratification, expressed as buoyancy frequency $N = \sqrt{-\frac{g}{\rho_o} \frac{\partial \rho}{\partial z}}$,
 340 exhibits a strong seasonal cycle at both the FRF and MVCO sites (Fig. 2a,b). Differences
 341 in the monthly means of stratification between the two locations are due in part to method-
 342 ological differences. At MVCO, monthly means of stratification are estimated from den-

343 sity differences at moored sensors between 1-4.5 m at the 7 m site, and between 1-9.5 m at
344 the 12 m site (Fig. 2b, solid lines). At FRF, stratification is estimated from density differ-
345 ences between 1-7 m from CTD casts conducted during the day, when higher stratification
346 is expected due to the daily cycle of surface heat flux (2a, solid lines). Using the climatol-
347 ogy of the daily maximum at the 7 m site at MVCO, in an attempt to account for daytime
348 sampling bias and differences in bottom depth, still indicates that the FRF site is typically
349 more stratified during all times of the year (Fig. 2b, dashed line). Weaker stratification at
350 MVCO may be due to mixing driven by stronger tidal currents. At both locations, highest
351 levels of stratification occur during the months of June-August. The analysis of nonlinear
352 momentum fluxes focuses primarily on these months.

353 Differences in wind forcing between FRF and MVCO also contribute to differences in
354 physical dynamics (Fig. 2c,d). At FRF, during the months of June-August, wind stress is
355 most commonly oriented offshore (positive τ^{sx}) and upwelling favorable (positive τ^{sy}). At
356 MVCO, wind stress is most commonly oriented with onshore τ^{sx} , but upwelling favorable
357 τ^{sy} . Wind stresses are not strongly polarized in the alongshore direction at either site,
358 unlike many locations on the US west coast where the winds are steered by coastline
359 topography.

360 The relationship between alongshore wind stress and cross-shelf transport differs be-
361 tween FRF and MVCO during the stratified period of June-August. At FRF, periods of
362 offshore and upwelling favorable wind stress are typically associated with offshore surface
363 layer transport U_s , consistent with upwelling circulation (Fig. 3a). Reversals to onshore
364 and downwelling favorable wind stress at this site are typically associated with onshore
365 U_s . The relationship between wind forcing and cross-shelf transport is more complex at
366 MVCO, where offshore U_s is typically present during a wide range of wind conditions
367 (Fig. 3b). Offshore U_s at this site is observed during onshore and upwelling-favorable
368 wind forcing, as well as reversals to offshore and downwelling favorable conditions. Weak
369 onshore U_s is present some of the time during onshore and downwelling favorable wind

370 stress, and during events in which wind stress is directly onshore with no alongshore com-
371 ponent. However, the magnitude of onshore U_s at MVCO is not as high as that observed
372 during similar wind conditions at FRF.

373 A subset of the FRF time series from 2013 is now used to describe wind forcing
374 and circulation patterns at time scales of days–weeks (Fig. 4). In the next section, it
375 will be shown that these circulation patterns influence the momentum balance through the
376 cross-shelf divergence of nonlinear momentum fluxes. Data from the FRF site are used to
377 present these patterns in time series form due to the relatively clear relationship between
378 cross-shelf transport and wind stress (Fig. 3). During the 45-day time period from 13-
379 June to 28-July 2013, wind stress typically varies between offshore, upwelling-favorable
380 conditions and onshore, downwelling favorable winds (Fig. 4a). Surface transport U_s
381 typically varies together at the three mooring sites from 5-8 m, increasing with offshore
382 distance (Fig. 4b). The reduction of U_s near the coast is a characteristic pattern of the inner
383 shelf region. Strong vertical shear in the alongshore current, $\partial v/\partial z$, is also present during
384 this time period at both the 6 m and 8 m sites (Fig. 4c). The vertical shear is estimated
385 from differences between 2.0-7.5 m at the 8 m site, and between 2.0-5.0 m depth at the
386 6 m site. Positive $\partial v/\partial z$ at both sites is generally associated with offshore U_s , as well
387 as offshore and upwelling favorable winds. The combination of vertical shear, cross-shelf
388 exchange and cross-shelf variations in the circulation provide the necessary conditions for
389 nonlinear terms to be potentially important in the alongshore momentum balance.

390 *b. Role of nonlinear terms in depth-averaged momentum balances*

391 The dynamical importance of the nonlinear momentum flux divergence is compared
392 with other terms in the depth-averaged alongshore momentum balance (equation 3). Com-
393 parisons of the magnitude and timing of the different terms are first made using the subset
394 of the time series at FRF (Fig. 4), then in a statistical analysis of all available data. The
395 nonlinear term, estimated from the 6 m and 8 m sites at FRF, is positive during much of
396 the 45-day period (Fig. 4d). When wind stress and the nonlinear term are both positive,

397 nonlinear momentum fluxes associated with upwelling circulation play a role in balancing
398 the wind stress. In this case, alongshore momentum is transferred to the ocean by the
399 surface stress, but there is a net offshore flux of alongshore momentum. There are also
400 events (e.g. at 22-June and 26-July) when the wind stress is downwelling-favorable, but
401 the nonlinear term is still positive. In this case, a net onshore flux of negative alongshore
402 momentum during downwelling reinforces negative τ^{sy} on the inner shelf.

403 The magnitude of the nonlinear term is comparable to other terms in the momentum
404 balance. Although the nonlinear term does not completely balance the wind stress during
405 the period of sustained upwelling-favorable winds from 24-June to 12-July, it is large
406 enough to make a dynamically important contribution (Fig. 4d). Bottom stress, estimated
407 using the logarithmic layer formulation, is also too small to balance wind stress during
408 this upwelling-favorable period (Fig. 4e). In contrast, the magnitude of the bottom stress
409 is larger than that of the wind stress during the downwelling favorable events at 22-June
410 and 26-July. These patterns are consistent with the contribution of a positive nonlinear
411 momentum flux divergence term during both upwelling and downwelling conditions.

412 Additional terms also play a role in the alongshore momentum balance. Acceleration
413 is important during certain periods of fluctuating bottom stress, which indicate reversals
414 in the direction of the alongshore flow (Fig. 4e). Estimates of the alongshore pressure gra-
415 dient are unavailable in this study, but drops in practical salinity below 30 do occur (Fig.
416 4f), indicating the presence of a buoyant plume originating at the mouth of the Chesapeake
417 Bay (Rennie et al., 1999; Lentz and Largier, 2006). The buoyant plume is associated with
418 southeastward flow and an alongshore pressure gradient force in the negative y direction.
419 The timing of the low-salinity events indicates that the alongshore pressure gradient con-
420 tributes to negative τ^{by} during periods of weak or upwelling-favorable wind stress, and
421 may also play a role during periods of large bottom stresses that exceed the downwelling-
422 favorable wind stress, in addition to the nonlinear momentum flux divergence.

423 Since wind stress and bottom stress have previously been identified as the dominant

424 terms in the alongshore momentum balance at FRF (Lentz et al., 1999), the role of the
425 nonlinear term in modifying the balance between these two terms is examined using all of
426 the available data at the 6 m and 8 m sites during June–August. The alongshore wind stress
427 is compared to three response variables: 1) bottom stress only (Fig. 5, BS); 2) the sum
428 of bottom stress and nonlinear momentum flux divergence (Fig. 5, BS+NL); and 3) the
429 sum of bottom stress, nonlinear momentum flux divergence and local acceleration (Fig.
430 5, BS+NL+A). Similar correlation coefficients of $r = 0.72$ - 0.77 are obtained for all three
431 response variables, although the correlations are slightly lower when the nonlinear term
432 is included in the response. Using a linear drag coefficient following Lentz et al. (1999)
433 yields a similar range of correlation coefficients, $r = 0.72$ - 0.75 (not shown). Despite the
434 similarity of the correlation coefficients obtained with different response variables, exam-
435 ining bin averages of the response by wind stress shows that the nonlinear term does have
436 an impact on the dynamical balance, and that this impact is greater than that of the ac-
437 celeration term (Fig. 5). Inclusion of the nonlinear terms results in a closer balance with
438 the wind stress. Consistent with the time series variability described above, the magni-
439 tude of the response is reduced for downwelling-favorable wind stress and increased for
440 upwelling-favorable wind stress when the nonlinear term is included. These asymmetric
441 changes under different wind conditions are not captured by linear regression analysis and
442 are not improved by tuning bottom drag coefficients.

443 To examine the role of wind forcing, the dependence of the nonlinear term on wind
444 stress is compared at the FRF and MVCO locations, focusing primarily on the stratified
445 period of June-August. At FRF, the response to wind stress is typically positive regardless
446 of whether τ^{sy} is positive or negative (Fig. 6a), consistent with the time series described
447 above at the same sites on the 6m and 8m isobaths (Figs. 4d, 5). The slopes of the re-
448 gressions between wind stress and nonlinear terms have the same sign when other pairs of
449 sites are examined; positive slopes are obtained for upwelling favorable wind stress and
450 negative slopes are obtained for downwelling favorable wind stress (Table 1). However,

451 the results obtained for downwelling favorable wind stress are less robust since the regres-
452 sion slopes are significantly different from zero for only three of the five pairs of sites. In
453 addition, the regression slope obtained for the shallowest sites at 5m and 6m during up-
454 welling favorable wind stress is only marginally significant, possibly due to the difficulty
455 in observing small differences in the momentum flux between sites in close proximity. In
456 general, these results from FRF during stratified period of June-August show that the non-
457 linear term is typically positive regardless of wind direction, but the correlation between
458 the nonlinear term and the alongshore wind stress is more consistent during periods of
459 upwelling favorable wind stress.

460 At MVCO, there is a different relationship between wind stress and the nonlinear
461 term. The nonlinear term at MVCO is positive for upwelling-favorable wind stress and
462 negative for downwelling-favorable wind stress (Fig. 6b). This different response to
463 downwelling-favorable winds at MVCO compared with FRF is consistent with the dif-
464 ferences in surface transport and cross-shelf wind stresses. The magnitude and direction
465 of the nonlinear term depends on both cross-shelf exchange, which can be quantified using
466 the surface transport, and the vertical structure of the alongshore flow, which can be quan-
467 tified using the vertical shear. At MVCO, an offshore surface transport is typically present
468 even when the alongshore component of wind stress is downwelling-favorable (Fig. 4d).
469 The strength and direction of vertical shear in the alongshore current, however, is sensi-
470 tive to the alongshore wind stress (Fewings et al., 2008). Variability of vertical shear in
471 response to alongshore wind stress and cross-shore density gradients will be examined in
472 greater detail in Section 2.d.

473 The magnitude of the nonlinear term relative to the wind stress also differs between
474 locations. The regression slope of 0.15 between the two terms at MVCO during June-
475 August is smaller than those obtained at FRF during upwelling favorable winds ((Fig. 6,
476 Table 1). Comparing the standard deviations of the two terms also shows that the nonlinear
477 term has a greater contribution to the momentum balance at FRF than MVCO (Fig. 7).

478 There are also consistent differences between seasons at each location (Fig. 7). At both
479 locations, the relative importance of the nonlinear term decreases during the months of
480 January–March when the water column is more weakly stratified (Fig. 2).

481 *c. Role of nonlinear terms in surface layer momentum balances*

482 The momentum balance integrated over the surface layer (equation 6) provides a
483 framework for linking nonlinear momentum fluxes to cross-shelf exchange and turbulent
484 stresses. As in the previous section, the roles of the nonlinear terms are compared be-
485 tween FRF and MVCO. The cross-shelf flux divergence is combined with the vertical flux
486 to show the net effect of nonlinear momentum fluxes integrated over the surface layer.

487 During the stratified months of June–August at FRF and MVCO, the alongshore wind
488 stress term is compared with two different response variables in the momentum balance of
489 the surface layer: 1) the Coriolis force (fU_s) and 2) the nonlinear terms. At FRF, the Cori-
490 olis force is correlated with the alongshore wind stress during both upwelling-favorable
491 and downwelling-favorable conditions (Fig. 8a). The regression slopes are significantly
492 less than one in each case, indicating that surface transport is significantly reduced from
493 the theoretical Ekman transport $U_{Ek} = \tau^{sy} / \rho_o f$ expected in deeper water. At MVCO, the
494 regression slope between the Coriolis force and wind stress during upwelling-favorable
495 conditions is smaller than at FRF (Fig. 8c). During downwelling-favorable wind stress at
496 MVCO, the regression slope is only marginally statistically significant but negative (Fig.
497 8c). This pattern is consistent with the persistent offshore transport that occurs at this
498 location, even during downwelling favorable wind stress (Fig. 3b).

499 At both locations, inclusion of the nonlinear terms impacts the alongshore momen-
500 tum balance of the surface layer. At FRF, similar to the depth-averaged momentum bal-
501 ance shown in Section 4.b, the relationship between the wind stress and the nonlinear
502 terms changes depending on the direction of the alongshore wind stress (Fig. 8b). During
503 upwelling-favorable winds at FRF, the positive regression slope between the wind stress
504 and the nonlinear terms (0.35 ± 0.15) indicates that a substantial fraction of the momen-

505 tum put into the ocean by wind stress is transferred offshore by the nonlinear momentum
506 fluxes associated with the upwelling circulation, in addition to being transferred downward
507 by the turbulent stress at the base of the surface layer (Fig. 8a). Based on the regression
508 coefficient, the impact of nonlinear momentum fluxes exceeds that of the Coriolis force.
509 Under downwelling favorable conditions at FRF, the regression slope is only marginally
510 different from zero (Fig. 8b). In this case, positive values of the nonlinear term are con-
511 sistent with a transfer of momentum from offshore by the nonlinear momentum fluxes
512 associated with the downwelling circulation, as well as an enhanced interior stress whose
513 magnitude exceeds that of the wind stress.

514 The nonlinear terms have a less significant impact on momentum balance of the sur-
515 face layer at MVCO, and once again there are differences from the dynamics observed at
516 FRF. At MVCO, the nonlinear terms tend to be positive during upwelling favorable winds
517 and negative during downwelling favorable winds (Fig. 8d). The regression slope is sig-
518 nificant, but the correlation of $r^2 = 0.27$ indicates substantial scatter in the relationship. A
519 piece-wise linear fit is only significant for the negative values of τ^{sy} . However, the over-
520 all trend is consistent with the depth averaged balance at the same site (Fig. 6b). Unlike
521 FRF, the nonlinear momentum fluxes at MVCO tend to balance the alongshore wind stress
522 during both upwelling-favorable and downwelling-favorable conditions. The presence of
523 persistent offshore surface transport at MVCO, even when the alongshore component of
524 wind stress is downwelling-favorable, alters the relationship between the nonlinear terms
525 and alongshore wind stress at this site. The influence of cross-shelf wind stress on surface
526 transport likely contributes to the variability of the nonlinear term, which depends in part
527 on the strength of cross-shore circulation.

528 *d. Role of density structure and processes influencing vertical shear*

529 Density stratification and cross-shelf density gradients can influence nonlinear mo-
530 mentum fluxes through their roles in governing mixing, cross-shelf exchange and vertical
531 shear. This section specifically focuses on the processes governing vertical shear in the

532 alongshore flow, which must be present for the nonlinear term to contribute to the along-
 533 shore momentum balance. There are several potential mechanisms for the generation of
 534 vertical shear, including thermal wind balance and frictional stresses. Hypothetical pre-
 535 dictions of vertical shear involving the cross-shelf density gradient and surface wind stress
 536 are now examined under different levels of stratification.

537 The hypothetical predictions are evaluated at the 7 m and 12 m sites at MVCO. The
 538 analysis focuses on depths where density and velocity data are available at both of these
 539 sites. Vertical shear is computed from velocity differences between 3 m and 5 m depths.
 540 The horizontal density gradient is computed from averages of density observations at
 541 depths of 3 m and 5 m at each site. Results are categorized based on the buoyancy fre-
 542 quency N , calculated from averages of the 7 m and 12 m sites. A value of $N = 0.01$
 543 s^{-1} is chosen to characterize periods of relatively weak and strong stratification. Based on
 544 climatological averages (Fig. 2b), periods of $N < 0.01 \text{ s}^{-1}$ are typical during October–
 545 March.

546 *i. Geostrophic shear and thermal wind balance* If the cross-shelf momentum balance
 547 is geostrophic, the vertical shear is proportional to the cross-shelf density gradient and
 548 determined by thermal wind balance

$$\frac{\partial v}{\partial z} = -\frac{g}{f\rho_o} \frac{\partial \rho}{\partial x}. \quad (8)$$

549 At MVCO, the cross-shelf density gradient $\partial\rho/\partial x$ is typically positive (density increases
 550 offshore), which is consistent with negative $\partial v/\partial z$ in a hypothetical thermal wind balance
 551 (Fig. 9a). During periods of weak stratification, $\partial\rho/\partial x$ is relatively small and sometimes
 552 negative. The two terms in the thermal wind balance are weakly correlated during both
 553 strongly stratified periods ($r = 0.44$, $p < 0.001$, slope = 0.55) and weakly stratified periods
 554 ($r = 0.51$, $p = 0.03$, slope = 0.37). However, there are times when there is clear disagree-
 555 ment. In particular, thermal wind balance fails to explain positive values of $\partial v/\partial z$. It

556 should be noted that comparing the terms of the thermal wind balance is challenging us-
 557 ing measurements from two moorings. The estimates of vertical shear at the 7m and 12m
 558 sites are only weakly correlated with each other ($r = 0.53$ during stratified periods, $r = 0.55$
 559 during unstratified periods) and small-scale density fronts may be unresolved. The agree-
 560 ment with thermal wind balance is not improved when the vertical shear from individual
 561 sites are used in place of the average, except when the 7m site is used during unstrati-
 562 fied periods (increasing r slightly from 0.51 to 0.55). Although unresolved gradients may
 563 be a factor, estimates from the available measurements suggest that there is substantial
 564 ageostrophic shear which is associated with deviations from thermal wind balance.

565 *ii. Wind-supported shear* In addition to geostrophic processes, which are inviscid and
 566 depend on the Earth's rotation, vertical shear can also be associated with the presence of
 567 turbulent stresses in the water column. To test whether the magnitude of the observed
 568 vertical shear $\partial v / \partial z$ is consistent with generation of frictional stresses by the wind, a
 569 hypothetical relationship based on a simple form of the eddy viscosity A is considered.
 570 Eddy viscosity over the inner shelf is expected to vary as a function of stratification, sur-
 571 face buoyancy fluxes, advection of the density field and distance from the boundaries.
 572 Although the data used in this study cannot resolve the complexity of turbulent stresses
 573 over the inner shelf, a simplified form of the eddy viscosity is used to compare the strength
 574 of hypothetical wind-supported shear relative to the geostrophic shear. In modeling a river
 575 plume under downwelling-favorable wind stress, Chen and Chen (2017) found the vertical
 576 shear to be consistent with the relationship

$$\frac{\partial v}{\partial z} = \frac{\tau^{sy}}{\rho_o A}, \quad (9)$$

577 where $A = \kappa u_* h / 6$, and $u_* = \sqrt{|\tau^s| / \rho_o}$ is a friction velocity based on the magnitude
 578 of the surface stress $|\tau^s|$. This provides an estimate of the depth-averaged shear when
 579 the alongshore stress $A \partial v / \partial z$ is constant throughout the water column and determined

580 completely by the wind stress. The choice of constant A is consistent with the depth-
581 average of a parabolic vertical profile of A (Chen and Chen, 2017). The hypothetical wind-
582 supported shear in equation (9) is expected to be most relevant when the water column is
583 unstratified.

584 Like the geostrophic shear, the hypothetical wind-supported shear alone cannot com-
585 pletely explain the observations (Fig. 9b). There is a significant correlation during periods
586 of weak stratification ($r = 0.74$, $p < 0.001$, slope = 0.40), but the expression for wind-
587 supported shear in equation (9) does not account for the presence of negative $\partial v / \partial z$ during
588 weak wind stress and the regression slope suggests that this relationship underestimates
589 the observed vertical shear. During stratified periods, the terms are also correlated ($r =$
590 0.71 , $p < 0.001$, slope = 1.41) but there are large discrepancies between the magnitudes of
591 the observed shear and theoretical predictions. Some of the negative $\partial v / \partial z$ values that are
592 inconsistent with the magnitude of the wind-supported shear can be explained by thermal
593 wind shear (Fig. 9a). Positive values of $\partial v / \partial z$ that cannot be explained by thermal wind
594 balance during periods relatively strong stratification occur during periods of positive τ^{sy}
595 and strong wind-supported shear (9b). It is therefore likely that the observed vertical shear
596 results from the combined effects of geostrophic and frictional processes.

597 *iii. Combined geostrophic and wind-supported shear* Cross-shelf density gradients
598 and wind stress both likely play a role in determining the strength and direction of the
599 vertical shear, and therefore the nonlinear fluxes of alongshore momentum. Stratification
600 also likely plays an important role in modulating vertical shear. Although thermal wind
601 balance does not completely explain the vertical shear at MVCO, the residual is signif-
602 icantly correlated with the alongshore wind stress during stratified periods (Fig. 10a, r
603 = 0.62, $p < 0.001$). Over the same range of alongshore wind stress values, variations
604 in vertical shear and the thermal wind balance residual are significantly reduced during
605 unstratified periods when cross-shelf density gradients are also relatively small (Figs. 9,
606 10a). These results suggest that the wind stress is most effective at generating ageostrophic

607 shear over the inner shelf when the water column is stratified.

608 The influences of stratification and cross-shelf density gradients on vertical shear are
609 important factors governing the dynamical importance of the cross-shelf momentum flux
610 divergence. The presence of vertical shear is essential for the nonlinear term in equation
611 (3) to have a role in the depth-averaged alongshore momentum balance. We conclude
612 this section by revisiting the relationship between the wind stress and the nonlinear term
613 at MVCO (Fig. 6b) and examining the influence of stratification. Consistent with the
614 results from June–August, the relationship between alongshore wind stress and vertical
615 shear, combined with upwelling circulation, leads to a weak but significant correlation
616 between along-shelf wind stress and the nonlinear term at MVCO when the water column
617 is stratified (Fig. 10b, $r = 0.44$, $p < 0.001$, slope = 0.18). However, during weakly
618 stratified time periods, the magnitude of the nonlinear term is much smaller over a similar
619 range of τ^{sy} values. Although the relationship between alongshore wind stress and the
620 nonlinear term differs between locations (Fig. 6), vertical shear is expected to vary in
621 response to thermal wind balance and alongshore wind stress at all inner shelf locations.

622 **5. Discussion**

623 *a. Circulation patterns associated with nonlinear momentum fluxes*

624 To summarize circulation patterns associated with nonlinear momentum fluxes over
625 the inner shelf, conceptual models are presented based on results from this study and
626 previous studies at the same locations (Fig. 11).

627 *i. North Carolina inner shelf* Flow patterns and dynamics associated with upwelling
628 circulation over the inner shelf are first described based on observations at the FRF site
629 (Fig. 11a). The most common wind pattern at FRF in North Carolina is upwelling fa-
630 vorable and offshore (Fig. 2c). This type of wind forcing is strongest before the passage
631 of an atmospheric front and is also associated with the strongest surface heat fluxes from
632 the atmosphere to the ocean (Austin and Lentz, 1999). As observed by Lentz (2001), the

633 magnitude of offshore U_s increases with water depth but typically remains less than the
634 theoretical deep water Ekman transport U_{Ek} at sites where water depth $h < 10$ m (Fig.
635 4b, 8a). The positive divergence of cross-shelf surface transport $\partial U_s / \partial x$ is consistent with
636 upward vertical velocity w_L over the inner shelf. Hydrographic observations offshore of
637 FRF during upwelling-favorable wind forcing in August show a shoaling of the thermo-
638 cline near shore (Austin and Lentz, 1999; 2002; Cudaback and Largier, 2001), which is
639 also consistent with the presence of an upwelling circulation.

640 Upwelling-favorable and offshore wind forcing at FRF is also often associated with
641 strong positive vertical shear $\partial v / \partial z$ (Fig. 11a). The vertical shear reaches similar values
642 at different mooring sites at FRF (Fig. 4c). The positive sign of $\partial v / \partial z$ is consistent with
643 thermal wind balance associated with negative $\partial \rho / \partial x$ as the thermocline shoals and cold,
644 dense water is upwelled near the coast. Density time series for estimating $\partial \rho / \partial x$ are not
645 available during the time period analyzed in this study, but previous observations show
646 significant correlations between the two terms in the thermal wind balance (Lentz et al.,
647 1999). However, Lentz et al. (1999) found weaker agreement with thermal wind balance
648 at the shallowest sites (8–13 m), and the largest disagreements appear to be during times
649 when $\partial v / \partial z$ is positive. In addition to geostrophic thermal wind shear, it is therefore
650 possible that wind forcing contributes directly to vertical shear by generating turbulent
651 stresses.

652 The circulation patterns established during upwelling-favorable and offshore wind
653 stress at FRF (Fig. 11a) lead to a divergence of the cross-shelf flux of alongshore momen-
654 tum, a nonlinear process that influences the alongshore momentum balance. The combi-
655 nation of offshore U_s and positive $\partial v / \partial z$ creates a net offshore flux of positive alongshore
656 momentum when integrated over the water column, $\int_{-h}^{\eta} (u_L v) dz$, since the onshore re-
657 turn flow in the lower layer is associated with relatively small v compared with the surface
658 layer. This flux increases with offshore distance as offshore transport increases and as the
659 surface-to-bottom velocity difference increases for similar $\partial v / \partial z$. This mechanism is sim-

660 ilar to that described by Lentz and Chapman (2004) for upwelling conditions at mid-shelf
661 locations. However, the dynamics are modified over the inner shelf because U_s changes
662 with offshore distance and there is no clear separation between the surface and bottom
663 boundary layers.

664 During downwelling-favorable and onshore wind forcing, the circulation patterns are
665 essentially reversed over the inner shelf at FRF (Fig. 11b). This type of wind forcing com-
666 monly follows the passage of atmospheric fronts (Austin and Lentz, 1999). The onshore
667 surface layer transport U_s is reduced from U_{Ek} , and there is a convergence $\partial U_s / \partial x < 0$
668 consistent with downward w_L (Lentz, 2001). Hydrographic data indicate the presence of a
669 downwelling front, with water of uniform temperature onshore of the front (Austin, 1999;
670 Cudaback and Largier, 2001). The cross-shelf circulation associated with downwelling
671 over the inner shelf is time-dependent, and has been shown in some cases to shut down af-
672 ter the downwelled isotherms move offshore (Lentz, 2001). However, the time-dependent
673 density structure can be complicated by the arrival of salinity associated with the Ches-
674 peake Bay freshwater plume, which lags negative (downwelling-favorable) τ^{sy} (Cudaback
675 and Largier, 2001). During weak or moderate downwelling-favorable wind stress, the
676 plume can promote stratification onshore of the downwelled isotherms and create a region
677 of positive $\partial \rho / \partial x$ and negative $\partial v / \partial z$ (Cudaback and Largier, 2001), which is qualita-
678 tively consistent with thermal wind balance. The vertical shear in the alongshore flow is
679 enhanced during periods of downwelling-favorable wind stress, which promotes mixing
680 of the plume during periods of relatively strong downwelling-favorable wind stress (Lentz
681 and Largier, 2006). The presence of mixing in the plume during both upwelling-favorable
682 and downwelling-favorable wind stress leads to ageostrophic shear and deviations from
683 thermal wind balance (Mazzini et al., 2019).

684 The circulation patterns associated with downwelling winds at FRF (Fig. 11b) lead to
685 a positive momentum flux divergence. This nonlinear term in the depth-averaged momen-
686 tum balance has the same positive sign during both upwelling and downwelling (Fig. 6a).

687 This is generally consistent with the idealized modeling study of Kuebel Cervantes et al.
688 (2004), in which the nonlinear terms make a mean positive contribution inshore of an up-
689 welling front under periodic wind forcing. Time dependence of the cross-shelf circulation,
690 and the presence of a freshwater plume, likely contribute to variability of this term during
691 downwelling-favorable winds.

692 *ii. New England inner shelf* At MVCO, the relationship between wind forcing and
693 nonlinear momentum flux divergence is less straightforward. During the stratified season
694 of June–August, winds are often either upwelling-favorable and onshore, or downwelling-
695 favorable and offshore (Fig. 2d). The wind stress components τ^{sy} and τ^{sx} therefore often
696 oppose each other in their contributions to U_s . Offshore U_s is present at MVCO during
697 a wide range of forcing conditions, including weak wind stress, consistent with the pres-
698 ence of a persistent mean upwelling circulation that has been previously identified at this
699 site (Fewings et al., 2008; Fewings and Lentz, 2011). Warmer, lighter water is typically
700 present near shore, consistent with observations of positive $\partial\rho/\partial x$ (Fig. 9a). Fewings and
701 Lentz (2011) show that the presence of warmer and lighter water near shore is consistent
702 with a combination of surface heat flux warming shallow waters and strong vertical mix-
703 ing. Compared with the North Carolina shelf, the New England shelf is characterized by
704 stronger tides, facilitating strong vertical mixing.

705 In the alongshore component of velocity, mean negative (westward) \bar{v} is present, likely
706 due to a combination of a large-scale mean alongshore pressure gradient (Lentz, 2008b;
707 Xu and Oey, 2011) and tidal rectification near shoals to the east of the mooring array
708 (Ganju et al., 2011; Kirincich et al., 2013). However, conditional averages of velocity
709 during alongshore wind forcing in winter months show that positive τ^{sy} in the range 0.5–
710 1.0 Pa is sufficient to reverse the alongshore flow to positive v , and create positive $\partial v/\partial z$
711 (Fewings et al., 2008). Conditional averages of velocity at MVCO during combined τ^{sy}
712 and τ^{sx} forcing and weak stratification show v in the same direction as the alongshore
713 component of wind stress (Kirincich, 2013). This pattern is consistent with model results

714 which show that alongshore wind stress is more effective than cross-shelf wind stress at
715 driving alongshore velocity (Tilburg, 2003). Reversals in alongshore velocity can occur
716 without a corresponding reversal in U_s at this location. However, prior studies that have
717 examined the vertical structure of alongshore currents under different wind conditions at
718 MVCO have primarily focused on periods of weak stratification.

719 In the stratified season at MVCO, during upwelling-favorable and onshore wind forc-
720 ing, circulation patterns are often characterized by offshore U_s and positive $\partial v/\partial z$ (Fig.
721 11c). The presence of positive $\partial v/\partial z$ is inconsistent with thermal wind balance and pos-
722 itive $\partial\rho/\partial x$ (Fig. 9a, Section 2.d.i). However, the presence of positive $\partial v/\partial z$ can be
723 explained by ageostrophic shear generated by the wind stress (Figs. 9b, 10). Deviations
724 from thermal wind balance are likely to occur over the inner shelf, where turbulent stresses
725 occur throughout the water column, which suggests that the theory developed for mid-shelf
726 locations by Lentz and Chapman (2004) does not fully explain the dynamics over the inner
727 shelf.

728 During downwelling-favorable and offshore wind forcing at MVCO, circulation pat-
729 terns are characterized by offshore U_s and negative $\partial v/\partial z$ (Fig. 11d). The presence of
730 negative $\partial v/\partial z$ can be attributed to a combination of thermal wind balance and wind-
731 induced shear (Figs. 9, 10a). During downwelling favorable winds at MVCO, this non-
732 linear term tends to balance negative τ^{sy} due to a net offshore flux of negative momentum
733 (Figs. 6b, 8d). This differs dramatically from downwelling-favorable conditions at FRF,
734 where a net onshore flux of negative momentum tends to reinforce the wind stress. These
735 results show that the contribution of the nonlinear momentum flux divergence depends on
736 the background circulation and cross-shelf component of wind stress, in addition to the
737 along-shelf wind stress.

738 *b. Dynamical importance of nonlinear momentum fluxes*

739 The observed relationships between the nonlinear terms and wind stress at FRF are
740 qualitatively consistent with the two-dimensional modeling study of Kuebel Cervantes

741 et al. (2003), which includes realistic wind forcing and surface fluxes during the time
742 period of the 1994 CoOP program. During upwelling favorable wind conditions in this
743 model study, the regression slopes between the nonlinear and wind stress terms in the
744 depth-averaged momentum balance are 0.26 at 4 m and 0.33 at 8 m. These regression
745 slopes are smaller than the value of 0.57 found in this study, but still account for an impor-
746 tant component of the momentum balance. During downwelling-favorable conditions, the
747 slopes obtained by Kuebel Cervantes et al. (2003) are negative, but with values of -0.037 to
748 -0.035, which are much smaller in magnitude than found here from the observations. Sim-
749 ilar to the observational estimates in this study (Fig. 5), the modeled momentum balance
750 shows different relationships between surface stress and bottom stress depending on the
751 sign of the alongshore wind stress. Neither this study nor the model study of Kuebel Cer-
752 vantes et al. (2003) account for the alongshore pressure gradient term in the momentum
753 balance, which Lentz et al. (1999) found to improve closure of the momentum balance
754 in the 1994 CoOP observations, although it was uncorrelated with the alongshore wind
755 stress. In addition to influencing the alongshore pressure gradient, the Chesapeake plume
756 also influences the FRF site by promoting density stratification and thermal wind shear
757 (Rennie et al., 1999; Cudaback and Largier, 2001). The presence of salinity stratifica-
758 tion likely increases cross-shelf exchange and alters the position of the downwelling front,
759 which may account for some of the differences between this study and the model study of
760 Kuebel Cervantes et al. (2003).

761 At MVCO, the nonlinear terms play a relatively minor role in balancing the along-
762 shore wind stress. In a previous study of the alongshore momentum balance at this
763 site, which does not include estimates of the nonlinear terms, Fewings and Lentz (2010)
764 demonstrated a dominant balance between the wind stress and the alongshore pressure
765 gradient, with bottom stress making a secondary contribution. Observations of the along-
766 shore pressure gradient are not available during the time period of the SWWIM observa-
767 tions used in this study. However, the regression slope of 0.15 between the wind stress and

768 the nonlinear term found in this study is significantly smaller than the regression slope of
769 0.9 between the wind stress and alongshore pressure gradient found by Fewings and Lentz
770 (2010). Although it is clearly not the dominant mechanism for balancing the wind stress at
771 MVCO, this contribution of the nonlinear term is likely greatest during periods of strong
772 stratification, when cross-shelf exchange and vertical shear are strongest.

773 *c. Estimation of nonlinear momentum flux divergence from a single moor-*
774 *ing*

775 It is possible to estimate the nonlinear term based on a single mooring, rather than a
776 pair of moorings, since there can be no flux of momentum at the coastal boundary. This
777 type of estimate has been used to justify neglecting the nonlinear term in previous studies
778 of the alongshore momentum balance at MVCO (Fewings and Lentz, 2010; Kirincich,
779 2013). If the vertically integrated momentum flux decreases linearly to the coast at $x = 0$,
780 the momentum flux divergence can be approximated as

$$\frac{\partial}{\partial x} \int_{-h}^0 (u_L v) dz \approx \frac{1}{x} \int_{-h}^0 (u_L v) dz. \quad (10)$$

781 The approximation in equation (10) was used by Lentz and Chapman (2004) to estimate
782 the momentum flux divergence from single moorings at mid-shelf sites. Over the inner
783 shelf, the observed variability of the depth-integrated momentum flux is consistent with
784 a monotonic decrease towards the coast (Fig. 12). Standard deviations of the depth-
785 integrated momentum flux during June–August are smaller at shallower water depths at
786 both FRF and MVCO. The standard deviations are larger at FRF than MVCO at similar
787 water depths, consistent with a greater importance of the momentum flux divergence term
788 over the North Carolina inner shelf.

789 To test the validity of the approximation in equation (10), the estimates made from
790 pairs of moorings are compared with the approximation estimated from the deeper moor-
791 ing only (Fig. 13a). The approximation is strongly correlated with the estimates made

792 from the pairs of moorings at FRF ($r = 0.92$) and MVCO ($r = 0.95$) during the stratified
793 months of June–August. However, the approximation in equation (10) underestimates the
794 magnitude of the nonlinear term estimated from pairs of moorings, as indicated by regres-
795 sion slopes of 2.1 at FRF and 1.5 at MVCO. This suggests that the assumption of a linear
796 decrease of the vertically integrated momentum flux near the coast may not be valid. This
797 is confirmed by comparing the standard deviation of the depth-integrated momentum flux
798 at different sites (Fig. 12). The variability is consistent with a quadratic increase with
799 water depth, from zero at the coast, which would result in an underestimate if a linear
800 increase is assumed. The approximation in equation (10) can be used to obtain an order of
801 magnitude estimate of the nonlinear term, and to examine how the nonlinear term varies
802 in time with the wind stress or other forcing, but it may represent a lower bound on the
803 value over the inner shelf.

804 *d. Factors governing importance of nonlinear momentum fluxes*

805 The dynamical impact of the nonlinear term is potentially significant, but this impact
806 varies both in time and between different inner shelf locations. To assess the factors that
807 govern the overall importance of nonlinear momentum fluxes, a scaling is developed based
808 on the bottom slope, surface transport and vertical shear. The expected role of the non-
809 linear term in the physical dynamics of the inner shelf is then discussed based on these
810 commonly observed parameters.

811 The scaling analysis assumes linear vertical profiles of u_L and v ,

$$u_L(z) = \frac{4U_s}{h} \left(1 + \frac{2z}{h} \right), \quad (11)$$

$$v(z) = v_s + \frac{\partial v}{\partial z} z, \quad (12)$$

812 where v_s is the surface velocity at $z = 0$. The linear cross-shelf velocity profile in equa-
813 tion (11) describes a two-layer flow that satisfies two-dimensional mass balance, $\bar{u}_L = 0$.

814 With the vertical structure of the velocity given by equations (11) and (12), the vertically-
 815 integrated cross-shelf flux of alongshore momentum is

$$\int_{-h}^0 (u_L v) dz = \frac{2}{3} U_s \frac{\partial v}{\partial z} h. \quad (13)$$

816 Three further simplifications are made about the cross-shelf structure of the circulation.
 817 First, the ratio of the surface transport U_s to the theoretical Ekman transport U_{Ek} is propor-
 818 tional to the ratio of the water depth h to the boundary layer depth δ_s , so that $U_s \propto U_{Ek} h / \delta_s$
 819 (Lentz and Fewings, 2012). Over the inner shelf, surface transport is reduced where the
 820 surface and bottom boundary layers overlap and $h < 2\delta_s$ (Lentz and Fewings, 2012). If
 821 the vertical shear $\partial v / \partial z$ and boundary layer depth δ_s are independent of h , the depth-
 822 integrated flux then depends on h^2 , consistent with the observed variability (Fig. 12).
 823 Second, a constant bottom slope is assumed so that $h = \alpha x$. With a constant bottom slope
 824 α , the surface transport increases with cross-shelf distance $U_s \sim U_{Ek} \alpha x / \delta_s$. Third, the
 825 vertical shear $\partial v / \partial z$ is assumed to be independent of h . With these simplifications, the
 826 vertically integrated momentum flux in equation (13) is proportional to x^2 , not x as as-
 827 sumed in the approximation in equation (10). Using these assumptions of the cross-shelf
 828 structure, the divergence of the nonlinear momentum flux is

$$\frac{\partial}{\partial x} \int_{-h}^0 (u_L v) dz = \frac{4}{3} \alpha U_s \frac{\partial v}{\partial z}. \quad (14)$$

829 This scaling highlights the three main factors that influence the magnitude and direction
 830 of the momentum flux divergence: 1) the cross-shelf transport U_s , 2) the vertical shear
 831 $\partial v / \partial z$, and 3) the bottom slope α . Note that the expression for the divergence of the
 832 nonlinear momentum flux in equation (14) does not change if the surface transport is
 833 driven primarily by the cross shelf component of the wind stress so that $U_s \propto -V_{Ek} h / \delta_s$,
 834 where $V_{Ek} = -\tau^{sx} / \rho_o f$, as expected for shallow depths $h < \delta_s$ (Lentz and Fewings,
 835 2012). In both cases, the surface transport increases linearly with water depth h in this

836 simplified scenario. If the alongshore flow is in geostrophic balance, the vertical shear
837 $\partial v/\partial z$ is related to the cross-shelf density gradient through thermal wind balance, as in
838 equation (8). However, the presence of turbulent stresses can introduce ageostrophic shear.
839 Ageostrophic shear contributes significantly to the total vertical shear in wind forced river
840 plumes (Chen and Chen, 2017; Mazzini et al., 2019). Estimates of the ageostrophic shear
841 at MVCO in this study are correlated with the alongshore wind stress at MVCO during
842 stratified conditions (Fig. 10a). It is therefore possible that a turbulent thermal wind
843 balance, in which geostrophic shear is modified by turbulent stresses, often applies over
844 the inner shelf where the water depth and boundary layer thickness are comparable.

845 To test whether the scaling in equation (13) summarizes the key dynamics of momen-
846 tum flux divergence over the inner shelf, estimates of the right-hand side are compared
847 with the momentum flux divergence diagnosed from pairs of moorings at FRF and MVCO
848 (Fig. 13b). Estimates of U_s and $\partial v/\partial z$ are obtained from the deeper mooring site in each
849 pair, while the bottom slope between the mooring pair at each location is used for α . The
850 scaling is significantly correlated with the nonlinear term, but overestimates the magni-
851 tude at both FRF ($r = 0.72$, $p < 0.001$, slope = 0.72) and MVCO ($r = 0.58$, $p < 0.001$,
852 slope = 0.44). The scaling is consistent with the much greater range in magnitude of the
853 nonlinear term at the FRF site compared with MVCO. Despite the highly simplified ver-
854 tical and cross-shelf structure on which it is based, the simple scaling agrees reasonably
855 well with the more detailed observational estimates, and can therefore be used to discuss
856 how different aspects of inner shelf circulation and site characteristics influence the role
857 of nonlinear processes.

858 To compare the importance of the nonlinear term at different inner shelf locations, it
859 is useful to relate its magnitude to the wind stress. The dynamical role of the nonlinear
860 term in the momentum balance can be summarized as a fraction of the alongshore wind
861 stress term,

$$\frac{\frac{\partial}{\partial x} \int_{-h}^0 (u_L v) dz}{\left(\frac{\tau^{sy}}{\rho_o} \right)} = \frac{4 \alpha U_s}{3 f U_{Ek}} \frac{\partial v}{\partial z}. \quad (15)$$

862 The fraction of theoretical Ekman transport in the surface layer, U_s/U_{Ek} , becomes part
 863 of this non-dimensional number. Close to the coast, the fraction of theoretical Ekman
 864 transport approaches zero. In the absence of an alongshore pressure gradient, the wind
 865 stress is rapidly balanced by bottom friction in these shallow depths. At the boundary of
 866 the inner shelf and mid shelf, where U_s/U_{Ek} approaches ~ 1 , the role of the nonlinear term
 867 is governed by α , f and $\partial v/\partial z$.

868 At the boundary of the inner shelf and mid shelf, the relationship between the non-
 869 linear term and the wind stress shares similarities with the theory developed by Lentz and
 870 Chapman (2004). This theory is based on assumptions that 1) the surface transport is
 871 equal to the theoretical Ekman transport, 2) thermal wind balance is valid, and 3) there is
 872 a relationship between the cross-shelf density gradient $\partial\rho/\partial x$ and the stratification $\partial\rho/\partial z$
 873 associated with isopycnals shoaling upward towards the coast. With these assumptions,
 874 the role of the nonlinear term in equation (15) could be summarized by the slope Burger
 875 number $S = N\alpha/f$ as in Lentz and Chapman (2004). Although the theory of Lentz and
 876 Chapman (2004) is based on a three-layer cross-shelf circulation structure, the presence of
 877 an inviscid interior between the surface and bottom boundary layers is not necessary for
 878 the nonlinear term to be important. However, a theory based on S may not be appropriate
 879 for inner shelf locations, which differ in important ways from the mid-shelf locations in
 880 eastern boundary upwelling systems examined by Lentz and Chapman (2004). At MVCO,
 881 there is positive cross-shelf density gradient $\partial\rho/\partial x$ and isopycnals slope downward toward
 882 the coast even during periods of upwelling-favorable τ^{sy} , which is inconsistent with the
 883 upward-sloping isopycnals assumed by Lentz and Chapman (2004). Kirincich and Barth
 884 (2009b) found that the importance of the nonlinear term in balancing the wind stress varied
 885 at different inner-shelf sites along the same isobath, due to differences in $\partial v/\partial z$ at

886 sites with similar stratification. In addition, compared with mid-shelf sites, thermal wind
887 balance is less well established over the inner shelf. Hydrographic sections and mooring
888 time series do show consistency with thermal wind balance in shallow water (Lentz et al.,
889 1999; Garvine, 2004; Kirincich and Barth, 2009a), indicating that it should play a strong
890 role in determining the vertical shear. At MVCO, thermal wind balance partially explains
891 variability in $\partial v/\partial z$, but does not account for positive $\partial v/\partial z$ during upwelling-favorable
892 wind stress (Section 4.d). Thermal wind balance may be more important at FRF where
893 stratification is stronger and $\partial v/\partial z$ varies over a wider range, although Lentz et al. (1999)
894 found this relationship to be weakest in shallow water.

895 Comparing the FRF and MVCO locations based on the three key factors of bottom
896 slope, surface transport and vertical shear helps explain differences in the magnitude and
897 relative importance of the nonlinear terms at each site. The regression slope between the
898 nonlinear term and the wind stress is 0.57 at FRF during upwelling-favorable wind stress,
899 and 0.15 at MVCO over all wind forcing conditions (Fig. 6). Differences in bottom slope
900 between the two locations, $\alpha = 6.4 \times 10^{-3}$ at FRF and $\alpha = 4.5 \times 10^{-3}$ at MVCO,
901 are relatively minor. For context, both of these values are in the middle of the range
902 of bottom slopes at the mid-shelf sites examined by Lentz and Chapman (2004), which
903 range from 1.5×10^{-3} to 10^{-2} . Although the continental shelf is relatively broad in the
904 Mid-Atlantic Bight, both mooring arrays examined in this study are located over steeper
905 nearshore bathymetry. Differences in f of $8.6 \times 10^{-5} \text{ s}^{-1}$ at FRF and $9.6 \times 10^{-5} \text{ s}^{-1}$ at
906 MVCO are also relatively minor. However, vertical shear and cross-shelf transport both
907 differ substantially between the FRF and MVCO locations. Values of $\partial v/\partial z$ vary between
908 -2.1×10^{-2} and $1.2 \times 10^{-2} \text{ s}^{-1}$ at MVCO (Fig. 9) but vary over a much larger range from
909 -7.0×10^{-2} to $7.0 \times 10^{-2} \text{ s}^{-1}$ at FRF (Fig. 4c). Based on regression slopes between
910 fU_s and τ^{sy}/ρ_0 during upwelling-favorable wind stress, the fraction of Ekman transport
911 U_s/U_{Ek} is 0.20 ± 0.08 at the 6–8m sites examined at FRF, and a much lower fraction 0.06
912 ± 0.03 at the 7–12m sites examined at MVCO despite their greater average depth (Fig.

913 8a,c). Differences in the role of the nonlinear terms at FRF and MVCO are best explained
914 by a combination of the strength of the cross-shelf circulation and the vertical shear in
915 the alongshore flow. Stronger vertical mixing associated with stronger tidal currents may
916 explain the lower fraction of Ekman transport (Castelao et al., 2010; e.g.) and weaker
917 vertical shear over the New England inner shelf.

918 The bottom slope can be an important parameter because it helps determine the cross-
919 shelf scale of the momentum flux divergence. For example, the nonlinear momentum
920 flux divergence has been found to play a major role in balancing the wind stress at sites
921 onshore of Heceta Bank over the Oregon inner shelf (Kirincich and Barth, 2009b). This
922 region has a relatively steep slope of $\alpha = 0.0125$, steeper than the two locations examined
923 in this study. Vertical shear estimated from a shipboard survey at this site gives $\partial v / \partial z \approx$
924 $1 \times 10^{-2} \text{ s}^{-1}$ (Kirincich and Barth, 2009a), which is similar to the magnitude observed
925 at MVCO (Fig. 10). At the 15m isobath off Oregon, where $U_s / U_{Ek} \approx 0.4$ (Kirincich
926 et al., 2005), equation (15) gives an estimate of ~ 0.67 for the ratio of the nonlinear and
927 wind stress terms. In contrast to this large influence of the nonlinear term over a steeply
928 sloping inner shelf, the influence of the nonlinear term is expected to be much smaller at
929 inner shelf locations with similar vertical shear but smaller bottom slopes. Over the west
930 Florida inner shelf, $\partial v / \partial z$ can reach values of $\sim 2 \times 10^{-2} \text{ s}^{-1}$ (Weisberg et al., 2001), but
931 the bottom slope of $\alpha \approx 8 \times 10^{-4}$ is relatively small. In this case, equation (15) gives an
932 upper bound of ~ 0.33 for the ratio of the nonlinear and wind stress terms at the boundary
933 of the inner shelf and mid-shelf, consistent with a relatively minor role of the nonlinear
934 terms in modeled alongshore momentum balances (Li and Weisberg, 1999; Weisberg et al.,
935 2001). Similarly, the nonlinear momentum flux divergence is also expected to play a
936 minor role over the New Jersey inner shelf, where $\alpha \approx 10^{-3}$ and $\partial v / \partial z$ reaches values
937 of $\sim 1 \times 10^{-2}$ (Garvine, 2004). Although a moderate value of $S \approx 0.7$ over the New
938 Jersey inner shelf suggests that nonlinear terms should be important based on the theory
939 of Lentz and Chapman (2004), equation (15) gives an upper bound of ~ 0.14 for the ratio

940 of the nonlinear and wind stress terms at the boundary of the inner shelf and mid-shelf.
941 Garvine (2004) did not estimate the magnitude of the nonlinear term, but bottom stress
942 was found to be substantial relative to the wind stress. Although the bottom slope plays
943 an important role in determining the importance of nonlinear momentum fluxes over the
944 inner shelf, dependence on the slope Burger number S may not be always applicable in
945 the same manner as mid-shelf sites in coastal upwelling regions.

946 The dynamical role of nonlinear momentum flux divergence is determined by a com-
947 plex set of interactions between stratification, turbulent mixing, cross-shelf exchange and
948 the alongshore flow, all of which are influenced by wind forcing. The nonlinear term
949 reaches greater magnitudes when stratification values of $N > 0.01 \text{ s}^{-1}$ are present at
950 MVCO (Fig. 10b). Stratification promotes cross-shelf exchange by reducing the bound-
951 ary layer thickness and the turbulent stress at the base of the surface layer. Stratification
952 can also promote the development of vertical shear by inhibiting shear instability. In addi-
953 tion to vertical density stratification, the cross-shelf density gradient has also been shown
954 to influence mixing and exchange when the inner shelf is forced by cross-shelf wind stress
955 (Horwitz and Lentz, 2014). The cross-shelf density gradient also influences vertical shear
956 of the alongshore flow through thermal wind balance. Cross-shelf fluxes of alongshore
957 momentum are therefore coupled with the cross-shelf advection of density. Cross-shelf
958 fluxes of alongshore momentum can also influence mixing by reducing the role of bottom
959 friction on the inner shelf, which can then promote near-bottom stratification in a positive
960 feedback mechanism.

961 A limitation of this study is that that it does not account for the three dimensional
962 aspects of the inner shelf circulation. Alongshore pressure gradients are an important
963 component of the alongshore momentum balances at FRF and MVCO (Lentz et al., 1999;
964 Fewings and Lentz, 2010), but observational estimates are not available concurrent with
965 the observations presented in this study. At FRF, the alongshore pressure gradient is un-
966 correlated with the alongshore wind stress and is driven in part by Chesapeake Bay plume

967 events (Lentz et al., 1999). The low salinity signature of the plume is evident in Fig. 4f
968 and the unresolved pressure gradient contributes to unresolved variance in the momentum
969 balance analysis. In contrast, at MVCO, the alongshore pressure gradient largely balances
970 the local wind stress, likely due to the effects of topography (Fewings and Lentz, 2010).
971 Inclusion of an alongshore pressure gradient in the theory of Lentz and Chapman (2004)
972 does not alter the dependence of the nonlinear term on the slope Burger number over
973 the mid-outer shelf. Similarly, even if there is a substantial alongshore pressure gradient
974 over the inner shelf, it cannot completely balance the wind stress if there is a cross-shelf
975 momentum flux divergence associated with cross-shelf circulation and vertically-sheared
976 alongshore flow.

977 Alongshore variations in velocity associated with three dimensional circulation pat-
978 terns, which are neglected in the simplified momentum balance in equation (3), may also
979 be significant. High-frequency radar observations of the surface circulation at MVCO sug-
980 gest that momentum fluxes associated with lateral exchange can be important near com-
981 plex bathymetry (Kirincich et al., 2013). Three dimensional processes may also affect the
982 nonlinear momentum fluxes associated with two-dimensional upwelling and downwelling
983 circulation patterns, which are the primary focus of this study. For example, Kumar and
984 Feddersen (2017) show that including transient rip currents in a numerical model of circu-
985 lation over a stratified inner shelf causes thermal wind balance to break down. Transient
986 rip currents over the inner shelf may therefore influence the vertical shear of the alongshore
987 flow, modulating the cross-shelf flux of alongshore momentum associated with upwelling
988 and downwelling. Submesoscale fronts over the inner shelf may be associated with along-
989 shore convergence, as well as alongshore variations in vertical shear $\partial v/\partial z$ (Dauhajre
990 et al., 2017; Wu et al., 2021). Because nonlinear processes can significantly influence the
991 alongshore momentum balance, studies of inner shelf dynamics should consider the poten-
992 tial for coupling between the dynamics of wind-driven circulation, submesoscale features
993 and wave-driven flow over the inner shelf.

994 An implication of this study is that the cross-shelf wind stress can play a role in the
995 alongshore momentum balance. The cross-shelf wind stress increases surface transport
996 U_s in shallow water, where alongshore wind stress is inefficient at driving cross-shelf ex-
997 change (Tilburg, 2003; Fewings et al., 2008). Increased surface transport increases the
998 magnitude of the nonlinear momentum flux divergence relative to the wind stress in the
999 scaling of the two terms in equation (15). However, cross-shelf wind stress alone does not
1000 drive significant alongshore flow (Tilburg, 2003), and therefore would not be expected to
1001 produce a strong momentum flux divergence. Combined offshore and upwelling-favorable
1002 wind stress, typical for the FRF site examined in this study, may provide optimal condi-
1003 tions for an important role of the nonlinear momentum flux divergence over the inner
1004 shelf.

1005 **6. Conclusion**

1006 The results of this study show that cross-shelf fluxes of alongshore momentum in-
1007 fluence the physical dynamics of the inner shelf. The two locations examined contrast
1008 strongly in the circulation patterns associated with nonlinear momentum fluxes, and their
1009 overall importance in the alongshore momentum balance. Over the North Carolina in-
1010 ner shelf, the momentum flux divergence plays an important role in balancing the along-
1011 shore wind stress during upwelling-favorable and offshore winds. During reversals to
1012 downwelling-favorable and onshore forcing, the momentum flux divergence acts in the
1013 same direction as the wind stress, allowing bottom stress to exceed the wind stress. Over
1014 the New England inner shelf, the importance of the momentum flux divergence is reduced,
1015 and tends to act in opposition to both upwelling-favorable and downwelling-favorable
1016 wind stress. These differences over the New England inner shelf are consistent with a
1017 combination of weaker stratification, weaker vertical shear, a background mean upwelling
1018 circulation, and cross-shelf wind stress that tends counteract the surface transport driven
1019 by alongshore wind stress.

1020 The role of the nonlinear momentum flux divergence should be taken into account at
1021 inner shelf locations characterized by strong vertical shear and steep bottom slope. The
1022 mechanism described in this study is similar to that described by Lentz and Chapman
1023 (2004) for mid-shelf sites. However, the relationship between wind forcing, stratification,
1024 the cross-shelf density gradient, turbulent mixing and vertical shear is complex over the
1025 inner shelf. This complexity is not captured by a simple dependence on the slope Burger
1026 number. In addition, because cross-shelf winds influence transport in the surface layer,
1027 the cross-shelf component of wind stress has the potential to influence the alongshore
1028 momentum balance over the inner shelf. The dynamics of the shallow inner shelf are
1029 often characterized by an overall balance between wind stress and bottom stress. However,
1030 nonlinear momentum fluxes can either reduce or increase the role of bottom stress relative
1031 to the wind stress, which affects the relationship between mixing and exchange over the
1032 inner shelf.

1033 *Acknowledgments.* We are grateful to all of the scientists, engineers and technicians at
1034 Woods Hole Oceanographic Institution and the Army Corps of Engineers Field Research
1035 Facility who contributed to the collection of time series data analyzed in this study. This
1036 analysis would not have been possible without the great effort involved in collecting high-
1037 quality observations over multiple years. Current meter and water property data from the
1038 North Carolina inner shelf are publicly available at <http://www.frf.usace.army.mil>. Data
1039 are provided by the Field Research Facility, Coastal Observations & Analysis Branch,
1040 US Army Corps of Engineers, Duck, North Carolina. Current meter and water property
1041 data from the New England inner shelf are publicly available from the Woods Hole Open
1042 Access Server (Lentz, 2021). Support for this work was provided by the National Science
1043 Foundation (OCE-1433716 and OCE-1558874). We thank the two reviewers for their
1044 helpful feedback.

1045

REFERENCES

1046

1047 Austin, J. A. 1999. The role of the alongshore wind stress in the heat budget of the
1048 North Carolina inner shelf. *J. Geophys. Res. Ocean.*, *104*(C8), 18187–18203. doi:
1049 10.1029/1998JC900122.

1050 Austin, J. A. and S. J. Lentz. 1999. The relationship between synoptic weather systems
1051 and meteorological forcing on the North Carolina inner shelf. *J. Geophys. Res. Ocean.*,
1052 *104*(C8), 159–185. doi: 10.1029/1999JC900016.

1053 Austin, J. A. and S. J. Lentz. 2002. The inner shelf response to wind-driven upwelling
1054 and downwelling. *J. Phys. Ocean.*, *32*, 2171–2193.

1055 Castelao, R., R. Chant, S. Glenn, and O. Schofield. 2010. The effects of tides and oscil-
1056 latory winds on the subtidal inner-shelf cross-shelf circulation. *J. Phys. Oceanogr.*, *40*
1057 (4), 775–788. doi: 10.1175/2009JPO4273.1.

1058 Chen, S.-Y. and S.-N. Chen. 2017. Generation of upwelling circulation under
1059 downwelling-favorable wind within bottom-attached, buoyant coastal currents. *J. Phys.*
1060 *Oceanogr.*, *47*(10), 2499–2519. doi: 10.1175/JPO-D-16-0271.1.

1061 Codiga, D. 2011. Unified tidal analysis and prediction using the
1062 UTide Matlab functions. Technical report, Graduate School of
1063 Oceanography, University of Rhode Island, Narragansett, RI. URL
1064 <http://www.po.gso.uri.edu/codiga/utide/utide.htm>.

1065 Cudaback, C. N. and J. L. Largier. 2001. The cross-shelf structure of wind- and buoyancy-
1066 driven circulation over the North Carolina inner shelf. *Cont. Shelf Res.*, *21*(15), 1649–
1067 1668. doi: 10.1016/S0278-4343(01)00025-5.

1068 Dauhajre, D. P., J. C. McWilliams, and Y. Uchiyama. 2017. Submesoscale coher-
1069 ent structures on the continental shelf. *J. Phys. Oceanogr.*, *47*(12), 2949–2976. doi:
1070 10.1175/JPO-D-16-0270.1.

- 1071 Feddersen, F., R. T. Guza, S. Elgar, and T. H. C. Herbers. 1998. Alongshore momen-
1072 tum balances in the nearshore. *J. Geophys. Res. Ocean.*, *103*(C8), 15667–15676. doi:
1073 10.1029/98JC01270.
- 1074 Fewings, M., S. J. Lentz, and J. Fredericks. 2008. Observations of cross-shelf flow driven
1075 by cross-shelf winds on the inner continental shelf. *J. Phys. Oceanogr.*, *38*, 2358–2378.
- 1076 Fewings, M. R. and S. J. Lentz. 2010. Momentum balances on the inner continental shelf
1077 at Martha’s Vineyard Coastal Observatory. *J. Geophys. Res. Ocean.*, *115*(12), C12023.
1078 doi: 10.1029/2009JC005578.
- 1079 Fewings, M. R. and S. J. Lentz. 2011. Summertime cooling of the shallow continental
1080 shelf. *J. Geophys. Res. Ocean.*, *116*(C7). doi: 10.1029/2010JC006744.
- 1081 Ganju, N. K., S. J. Lentz, A. R. Kirincich, and J. T. Farrar. 2011. Complex mean circu-
1082 lation over the inner shelf south of Martha’s Vineyard revealed by observations and a
1083 high-resolution model. *J. Geophys. Res.*, *116*, C10036. doi: 10.1029/2011JC007035.
- 1084 Garvine, R. W. 2004. The vertical structure and subtidal dynamics of the inner shelf off
1085 New Jersey. *J. Mar. Res.*, *62*(3), 337–371. doi: 10.1357/0022240041446182.
- 1086 Grifoll, M., A. L. Aretxabaleta, M. Espino, and J. C. Warner. 2012. Along-shelf current
1087 variability on the Catalan inner-shelf (NW Mediterranean). *J. Geophys. Res. Ocean.*,
1088 *117*(C9). doi: 10.1029/2012JC008182.
- 1089 Hickey, B. M. 1989. Patterns and processes of circulation over the Washington continental
1090 shelf and slope. In Landry, M. R. and B. M. Hickey, editors, *Coastal Oceanography of*
1091 *Washington and Oregon*, pages 41–115. Elsevier.
- 1092 Horwitz, R. and S. J. Lentz. 2014. Inner-shelf response to cross-shelf wind stress: The
1093 importance of the cross-shelf density gradient in an idealized numerical model and field
1094 observations. *J. Phys. Oceanogr.*, *44*(1), 86–103. doi: 10.1175/JPO-D-13-075.1.

- 1095 Horwitz, R. M. and S. J. Lentz. 2016. The effect of wind direction on cross-shelf
1096 transport on an initially stratified inner shelf. *J. Mar. Res.*, *74*, 201–227. doi:
1097 10.1357/002224016820870648.
- 1098 Kirincich, A. R. 2013. Long-term observations of turbulent Reynolds stresses over the
1099 inner continental shelf. *J. Phys. Oceanogr.*, *43*(12), 2752–2771. doi: 10.1175/JPO-D-
1100 12-0153.1.
- 1101 Kirincich, A. R. and J. A. Barth. 2009a. Time-varying across-shelf Ekman transport and
1102 vertical eddy viscosity on the inner shelf. *J. Phys. Oceanogr.*, *39*, 602–620.
- 1103 Kirincich, A. R. and J. A. Barth. 2009b. Alongshelf variability of inner-shelf circulation
1104 along the central Oregon coast during summer. *J. Phys. Oceanogr.*, *39*(6), 1380–1398.
1105 doi: 10.1175/2008JPO3760.1.
- 1106 Kirincich, A. R., J. A. Barth, B. A. Grantham, B. A. Menge, and J. Lubchenco. 2005.
1107 Wind-driven inner-shelf circulation off central Oregon during summer. *J. Geophys.*
1108 *Res.*, *110*(10), C10S03. doi: 10.1029/2004JC002611.
- 1109 Kirincich, A. R., S. J. Lentz, J. T. Farrar, and N. K. Ganju. 2013. The spatial structure
1110 of tidal and mean circulation over the inner shelf south of Martha’s Vineyard, Mas-
1111 sachusetts. *J. Phys. Oceanogr.*, *43*(9), 1940–1958. doi: 10.1175/JPO-D-13-020.1.
- 1112 Kuebel Cervantes, B. T., J. S. Allen, and R. M. Samelson. 2003. A modeling study of
1113 Eulerian and Lagrangian aspects of shelf circulation off Duck, North Carolina. *J. Phys.*
1114 *Oceanogr.*, *33*(10), 2070–2092.
- 1115 Kuebel Cervantes, B. T., J. S. Allen, and R. M. Samelson. 2004. Lagrangian characteristics
1116 of continental shelf flows forced by periodic wind stress. *Nonlinear Process. Geophys.*,
1117 *11*(1), 3–16. doi: 10.5194/npg-11-3-2004.

- 1118 Kumar, N. and F. Feddersen. 2017. The effect of Stokes drift and transient rip currents
1119 on the inner shelf. Part II: With stratification. *J. Phys. Oceanogr.*, *47*(1), 243–260. doi:
1120 10.1175/JPO-D-16-0077.1.
- 1121 Lee, G.-h., C. T. Friedrichs, and C. E. Vincent. 2002. Examination of diffusion ver-
1122 sus advection dominated sediment suspension on the inner shelf under storm and
1123 swell conditions, Duck, North Carolina. *J. Geophys. Res.*, *107*(C7), 3084. doi:
1124 10.1029/2001JC000918.
- 1125 Lentz, S. J. 1995. Sensitivity of the inner-shelf circulation to the form of the eddy viscosity
1126 profile. *J. Phys. Oceanogr.*, *25*, 19–28.
- 1127 Lentz, S. J. 2001. The influence of stratification on the wind-driven cross-shelf cir-
1128 culation over the North Carolina shelf. *J. Phys. Oceanogr.*, *31*(9), 2749–2760. doi:
1129 10.1175/1520-0485(2001)031;2749:TIOSOT;2.0.CO;2.
- 1130 Lentz, S. J. 2008a. Seasonal variations in the circulation over the Middle Atlantic Bight
1131 continental shelf. *J. Phys. Oceanogr.*, *38*, 1486–1500. doi: 10.1175/2007JPO3767.1.
- 1132 Lentz, S. J. 2008b. Observations and a model of the mean circulation over the
1133 Middle Atlantic Bight continental shelf. *J. Phys. Oceanogr.*, *38*, 1203–1221. doi:
1134 10.1175/2007JPO3768.1.
- 1135 Lentz, S. J. 2021. Dataset: Stratification, Wind, and Waves on the In-
1136 ner shelf of Martha’s Vineyard (SWWIM). WHOAS: Woods Hole Open Ac-
1137 cess Server. Last modified 8 June 2021. doi: 10.26025/1912/27252. URL
1138 <https://hdl.handle.net/1912/27252>.
- 1139 Lentz, S. J. and D. C. Chapman. 2004. The importance of the nonlinear cross-shelf
1140 momentum flux during wind-driven coastal upwelling. *J. Phys. Oceanogr.*, *34*(11),
1141 2444–2457.

- 1142 Lentz, S. J. and M. R. Fewings. 2012. The wind- and wave-driven inner-shelf circulation.
1143 *Ann. Rev. Mar. Sci.*, *4*, 317–343. doi: 10.1146/annurev-marine-120709-142745.
- 1144 Lentz, S. J., M. Fewings, P. Howd, J. Fredericks, and K. Hathaway. 2008. Observations
1145 and a model of undertow over the inner continental shelf. *J. Phys. Oceanogr.*, *38*(11),
1146 2341–2357. doi: 10.1175/2008JPO3986.1.
- 1147 Lentz, S., R. T. Guza, S. Elgar, F. Feddersen, and T. H. C. Herbers. 1999. Momentum
1148 balances on the North Carolina inner shelf. *J. Geophys. Res. Ocean.*, *104*(C8), 18205–
1149 18226. doi: 10.1029/1999JC900101.
- 1150 Lentz, S. J. and J. Largier. 2006. The influence of wind forcing on the Ches-
1151 peake Bay buoyant coastal current. *J. Phys. Oceanogr.*, *36*(2005), 1305–1316. doi:
1152 10.1175/JPO2909.1.
- 1153 Li, Z. and R. H. Weisberg. 1999. West Florida continental shelf response to upwelling
1154 favorable wind forcing 2. Dynamics. *J. Geophys. Res.*, *104*(C10), 23427–23442.
- 1155 Liu, Y. and R. H. Weisberg. 2005. Momentum balance diagnoses for the West Florida
1156 Shelf. *Cont. Shelf Res.*, *25*(17), 2054–2074. doi: 10.1016/j.csr.2005.03.004.
- 1157 Mazzini, P. L., R. J. Chant, M. E. Scully, J. Wilkin, E. J. Hunter, and N. J. Nidzieko. 2019.
1158 The impact of wind forcing on the thermal wind shear of a river plume. *J. Geophys.*
1159 *Res. Ocean.*, *124*(11), 7908–7925. doi: 10.1029/2019JC015259.
- 1160 Mitchum, G. T. and A. J. Clarke. 1986. The frictional nearshore response to forcing by
1161 synoptic scale winds. *J. Phys. Oceanogr.*, *16*(5), 934–946.
- 1162 Monismith, S. G. and D. A. Fong. 2004. A note on the potential transport of
1163 scalars and organisms by surface waves. *Limnol. Oceanogr.*, *49*(4), 1214–1217. doi:
1164 10.4319/lo.2004.49.4.1214.

- 1165 Moody, J. A., B. Butman, R. C. Beardsley, W. S. Brown, P. Daifuku, J. D. Irish, D. A.
1166 Mayer, H. O. Mofjeld, B. Petrie, S. Ramp, P. Smith, and W. R. Wright. 1984. At-
1167 las of tidal elevation and current observations on the Northeast American continen-
1168 tal shelf and slope. Bulletin 1611. Technical report, U.S. Geological Survey. URL
1169 <http://pubs.er.usgs.gov/publication/b1611>.
- 1170 Ofsthun, C., X. Wu, G. Voulgaris, and J. C. Warner. 2019. Alongshore momentum balance
1171 over shoreface-connected ridges, Fire Island, NY,. *Cont. Shelf Res.*, *186*, 21–33. doi:
1172 [10.1016/j.csr.2019.07.005](https://doi.org/10.1016/j.csr.2019.07.005).
- 1173 Rennie, S. E., J. L. Largier, and S. J. Lentz. 1999. Observations of a pulsed buoy-
1174 ancy current downstream of Chesapeake Bay. *J. Geophys. Res.*, *104*(C8), 18227. doi:
1175 [10.1029/1999JC900153](https://doi.org/10.1029/1999JC900153).
- 1176 Rosenfeld, L. K. 1983. CODE-1: Moored array and large-scale data report, Technical
1177 Report 83-23, Woods Hole Oceanographic Institution. Technical report, Woods Hole
1178 Oceanographic Institution.
- 1179 Smith, J. A. 2006. Wave-current interactions in finite depth. *J. Phys. Oceanogr.*, *36*(7),
1180 1403–1419. doi: [10.1175/JPO2911.1](https://doi.org/10.1175/JPO2911.1).
- 1181 Smith, S. D. 1988. Coefficients for sea surface wind stress, heat flux, and wind profiles as
1182 a function of wind speed and temperature. *J. Geophys. Res. Ocean.*, *93*(C12), 15467–
1183 15472. doi: [10.1029/JC093iC12p15467](https://doi.org/10.1029/JC093iC12p15467).
- 1184 Thieler, E., D. Foster, D. Mallinson, E. Himmelstoss, J. McNinch, J. List, and E. Hammar-
1185 Klose. 2013. Quaternary geophysical framework of the northeastern North Car-
1186 olina coastal system: U.S. Geological Survey Open-File Report 2011-2015. URL
1187 <https://pubs.usgs.gov/of/2011/1015/>.
- 1188 Tilburg, C. E. 2003. Across-shelf transport on a continental shelf: Do across-shelf winds
1189 matter? *J. Phys. Oceanogr.*, *33*(12), 2675–2688.

- 1190 Uchiyama, Y., J. C. McWilliams, and A. F. Shchepetkin. 2010. Wave-current interaction
1191 in an oceanic circulation model with a vortex-force formalism: Application to the surf
1192 zone. *Ocean Model.*, *34*, 16–35. doi: 10.1016/j.ocemod.2010.04.002.
- 1193 Weisberg, R. H., Z. Li, and F. Muller-Karger. 2001. West Florida shelf response to local
1194 wind forcing: April 1998. *J. Geophys. Res. Ocean.*, *106*(C12), 31239–31262. doi:
1195 10.1029/2000JC000529.
- 1196 Woodson, C. B. 2013. Spatiotemporal variation in cross-shelf exchange across the in-
1197 ner shelf of Monterey Bay, California. *J. Phys. Oceanogr.*, *43*(8), 1648–1665. doi:
1198 10.1175/JPO-D-11-0185.1.
- 1199 Wu, X., F. Feddersen, and S. N. Giddings. 2021. Characteristics and dynamics of density
1200 fronts over the inner to midshelf under weak wind conditions. *J. Phys. Oceanogr.*, *51*
1201 (3), 789–808. doi: 10.1175/JPO-D-20-0162.1.
- 1202 Xu, F.-H. and L.-Y. Oey. 2011. The origin of along-shelf pressure gradient in the Middle
1203 Atlantic Bight. *J. Phys. Oceanogr.*, *41*(9), 1720–1740. doi: 10.1175/2011JPO4589.1.
- 1204 Xu, Z. and A. J. Bowen. 1994. Wave- and wind-driven flow in water of finite depth. *J.*
1205 *Phys. Oceanogr.*, *24*, 1850–1866.

Table 1: Results from piecewise linear regressions between wind stress and nonlinear terms in the depth averaged momentum balance over the North Carolina inner shelf during June-August. Analysis is restricted to time periods when each site is outside the surf zone and $\bar{u}_L < 0.03$ m/s. Regression slopes are given with 95% confidence intervals for both upwelling favorable wind stress (positive τ^{sy}) and downwelling favorable wind stress (negative τ^{sy}) at five different pairs of sites. Results from the 6m-8m sites are shown in Figure 6.

Sites	Upwelling favorable	Downwelling favorable
5m-6m	0.51 ± 0.5	-0.15 ± 0.6
5m-8m	0.5 ± 0.21	-0.38 ± 0.22
6m-8m	0.57 ± 0.21	-0.77 ± 0.51
6m-11m	0.87 ± 0.32	-0.46 ± 0.36
8m-11m	0.66 ± 0.4	-0.32 ± 0.33

1206 **List of Figures**

1207 1 a) Coastline and bathymetry of the Mid-Atlantic Bight region. Red squares
1208 indicate locations of long-term current meter arrays used in this study.
1209 Red triangle indicates location of long-term tide gauge at the mouth of
1210 Chesapeake Bay. Gray contours indicate isobaths at 20-m intervals out to
1211 200 m. b) Overview of FRF field site at Duck, NC, showing locations of
1212 current meters (circles), tide gauge (triangle) and meteorological observa-
1213 tions (square). Contours indicate isobaths at 2 m intervals, starting at the
1214 4 m isobath. Axes show average offshore (x) and upwelling-favorable (y)
1215 coordinate system orientation determined from principal axis analyses of
1216 current meter data. Length of arrows depicts horizontal scale of 300 m.
1217 c) Overview of MVCO field site at Martha’s Vineyard, MA, showing lo-
1218 cations of current meters at the 7 m and 12 m isobaths from the SWWIM
1219 project (circles) and MVCO beach meteorological observations (square).
1220 Contours indicate isobaths at 2 m intervals, starting at the 2m isobath.
1221 Coordinate system and scales as in panel b. 55

1222	2	Comparison of stratification (a, b) and wind stress (c,d) at the FRF site in Duck, NC (left column) and Martha’s Vineyard, MA (right column). a) Monthly averages of buoyancy frequency, N , calculated from daily vertical profiles at the end of the FRF pier (black circles). Line shows seasonal climatology computed from monthly averages. b) Monthly averages and seasonal climatology of N computed from all SWWIM mooring observations at the 7 m site (gray circles and solid line) and 12 m site (black circles and solid line). Monthly averages and climatology of N computed from daily maxima at the 7 m site are also shown (gray triangles and dashed line). c) Wind rose plot for FRF site, showing frequency of occurrence of wind stress magnitude (N/m^2) and direction at FRF site during the months of June-August. The coordinate system has been rotated relative to offshore (x) and upwelling-favorable (y) coordinates shown in Figure 1b. d) As in panel c, for MVCO site and coordinate system shown in Figure 1c.	56
1236	3	Cross-shelf and along-shelf components of wind stress (τ^{sx}, τ^{sy}) during the months of June-August, with colors indicating surface transport U_s at a) FRF, and b) MVCO. Each point represents a 33-hour average of low-pass filtered data.	57

1240	4	Time series at FRF during the 45-day period 13 June–28 July 2013. a)	
1241		Cross-shore (red) and alongshore (blue) components of wind stress. b)	
1242		Cross-shore surface transport, U_S , at the 8 m (black), 6 m (dark gray) and	
1243		5 m (light gray) sites. c) Vertical shear in alongshore currents, $\partial v/\partial z$, at	
1244		the 6 m and 8 m sites. d) Selected terms in the depth-integrated alongshore	
1245		momentum balance, averaged between the 6 m and 8 m sites: wind stress	
1246		($\tau^{sy}/\rho_o D$, blue) and nonlinear advection ($1/D\partial/\partial x \int_{-h}^{\eta}(u_L v)dz$, red). e)	
1247		Selected terms in the depth-integrated alongshore momentum balance, av-	
1248		eraged between the 6 m and 8 m sites: wind stress ($\tau^{sy}/\rho_o D$, blue) and	
1249		logarithmic bottom stress ($\tau^{by}/\rho_o D$, black). f) Practical salinity, S_P , from	
1250		CTD casts at a depth of 1 m.	58
1251	5	Comparison of wind stress, bottom stress and nonlinear advection terms	
1252		in the depth-averaged alongshore momentum balance at FRF during June–	
1253		August. Wind stress term vs. bottom stress (BS) term (blue); wind stress	
1254		term vs. sum of bottom stress and nonlinear (BS + NL) terms (red); and	
1255		wind stress term vs. sum of bottom stress, nonlinear and acceleration (BS	
1256		+ NL + A) terms (black). Each circle represents a 33-hour average of low-	
1257		pass filtered data. Squares are bin averages, with vertical lines showing	
1258		standard errors.	59
1259	6	Comparison of wind stress and nonlinear advection terms in the along-	
1260		shore momentum balance during June–August. a) At FRF over the North	
1261		Carolina inner shelf. Red lines indicate results of piecewise linear regres-	
1262		sions of the 33-hour subsampled values, one regression for positive values	
1263		of wind stress and another for negative values of wind stress. b) At MVCO	
1264		over the New England inner shelf. One linear regression is used for both	
1265		positive and negative values of wind stress. Note difference in scale be-	
1266		tween panels a and b.	60

1267	7	Comparison of variability in the nonlinear and wind stress terms in the	
1268		alongshore momentum balance. a). Ratio of standard deviations of the	
1269		nonlinear term and wind stress term at FRF over the North Carolina inner	
1270		shelf. Black bars show ratios during June–August and gray bars show	
1271		ratios during January–February. Ratios are shown for five different pairs	
1272		of sites. Vertical lines indicate 95% confidence intervals. b) As in panel a,	
1273		for three pairs of sites at MVCO over the New England inner shelf.	60
1274	8	Comparison of wind stress, Coriolis and nonlinear advection terms in	
1275		the surface layer-integrated alongshore momentum balance at FRF dur-	
1276		ing June–August. a) Wind stress term vs. Coriolis terms at FRF. Each	
1277		circle indicates a 33-hour average of low-pass filtered data. Lines indicate	
1278		separate linear regression fits for positive and negative wind stress val-	
1279		ues. Regression slopes are shown with 95% confidence intervals. b) As in	
1280		panel a, for wind stress term vs. nonlinear terms at FRF. c) As in panel a,	
1281		for wind stress term vs. Coriolis term at MVCO. d) As in panel a, for wind	
1282		stress term vs. nonlinear terms at MVCO, and with one linear regression	
1283		fit for all data points.	61
1284	9	Evaluation of processes governing vertical shear, $\partial v/\partial z$, at MVCO. a)	
1285		Hypothetical vertical shear associated with thermal wind balance in equa-	
1286		tion (8). Circles indicate relatively strong stratification, $N > 0.01$. Trian-	
1287		gles indicate relatively weak stratification, $N \leq 0.01$. Black dashed line	
1288		indicates 1:1 relationship. b) Hypothetical vertical shear associated with	
1289		alongshore wind stress τ^{sy} and eddy viscosity $A = \kappa u_* h/6$ in equation (9).	62

1290	10	a) Wind stress term $\tau^{sy}/(\rho_o h)$ vs. the thermal wind balance residual	
1291		$\partial v/\partial z + g/(f\rho_o)\partial\rho/\partial x$ at MVCO. Circles indicate relatively strong stratification, $N > 0.01$. Triangles indicate relatively weak stratification, $N \leq 0.01$.	
1292		b) Wind stress and nonlinear advection terms in the depth-averaged momentum balance at MVCO under different levels of stratification.	63
1293			
1294			
1295			
1296	11	Conceptual models of circulation patterns associated with nonlinear momentum fluxes at different locations and under different forcing conditions. Arrows represent cross-shelf and vertical vector components. Circles represent alongshore vector components (\otimes indicates wind stress or ocean velocity in the positive y direction). Dashed lines indicate isopycnals, where darker shading is relatively dense. a) FRF, upwelling-favorable and offshore wind stress. b) FRF, downwelling-favorable and onshore wind stress. c) MVCO, upwelling-favorable and onshore wind stress. d) MVCO, downwelling-favorable and offshore wind stress.	64
1297			
1298			
1299			
1300			
1301			
1302			
1303			
1304			
1305	12	Standard deviations of the depth-integrated nonlinear momentum flux as a function of water depth, for the months of June–August. Black symbols represent estimates from FRF and gray symbols represent estimates from MVCO. Vertical bars indicate 95% confidence intervals. Dashed lines show hypothetical dependence on ah^2 , where a is a constant coefficient obtained from a least squares fit at each location.	65
1306			
1307			
1308			
1309			
1310			

1311 13 Simplified representations of the nonlinear term in the depth-averaged mo-
1312 mentum balance. a) Comparison of the approximation in equation (10)
1313 estimated from single deeper mooring (x -axis) vs. full estimate from
1314 mooring pairs (y -axis). Black symbols represent estimates from the 6–8m
1315 sites at FRF and gray symbols represent estimates from the 7–12m sites at
1316 MVCO. Blacked dashed line represents 1:1 agreement. b) Comparison of
1317 the scaling in equation (13) estimated from single deeper mooring (x -axis)
1318 vs. full estimate from mooring pairs (y -axis). Symbols as in panel a. . . . 66

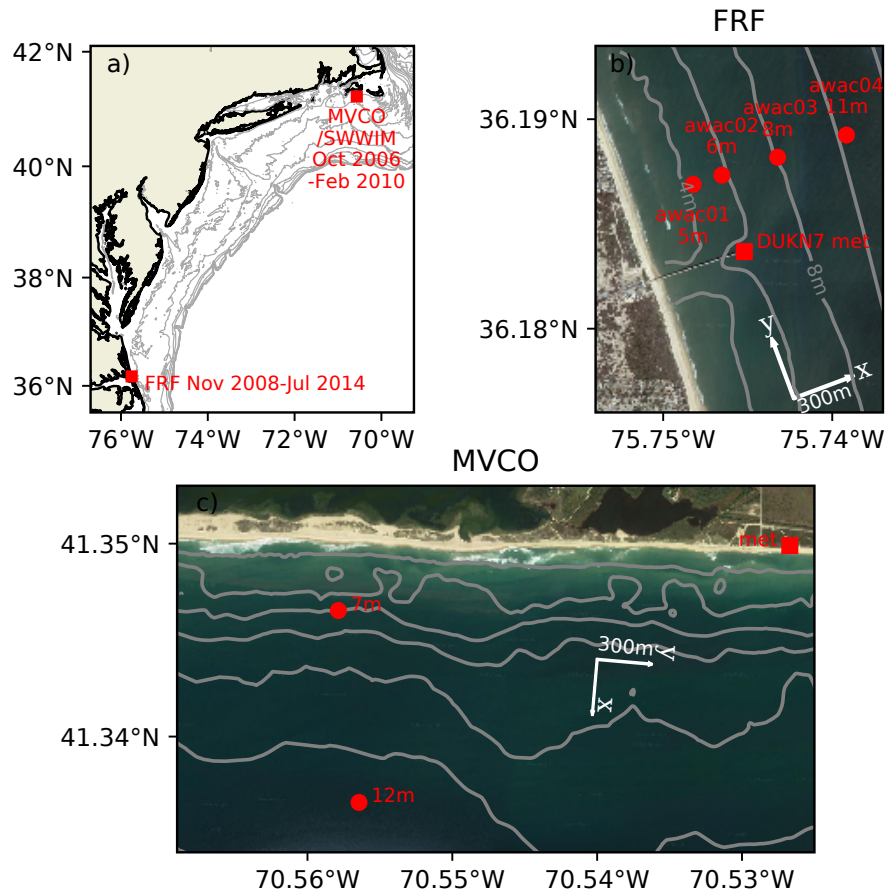


Figure 1: a) Coastline and bathymetry of the Mid-Atlantic Bight region. Red squares indicate locations of long-term current meter arrays used in this study. Red triangle indicates location of long-term tide gauge at the mouth of Chesapeake Bay. Gray contours indicate isobaths at 20-m intervals out to 200 m. b) Overview of FRF field site at Duck, NC, showing locations of current meters (circles), tide gauge (triangle) and meteorological observations (square). Contours indicate isobaths at 2 m intervals, starting at the 4 m isobath. Axes show average offshore (x) and upwelling-favorable (y) coordinate system orientation determined from principal axis analyses of current meter data. Length of arrows depicts horizontal scale of 300 m. c) Overview of MVCO field site at Martha's Vineyard, MA, showing locations of current meters at the 7 m and 12 m isobaths from the SWWIM project (circles) and MVCO beach meteorological observations (square). Contours indicate isobaths at 2 m intervals, starting at the 2m isobath. Coordinate system and scales as in panel b.

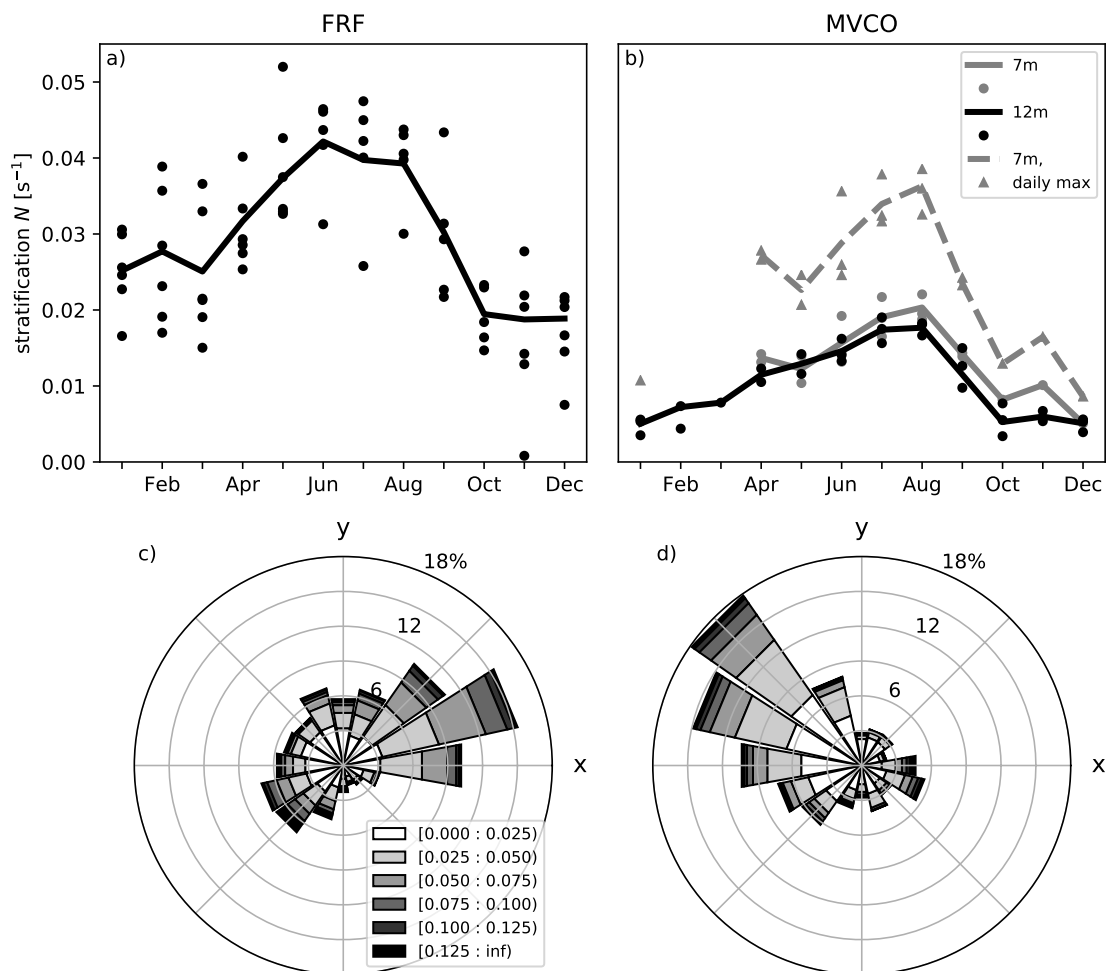


Figure 2: Comparison of stratification (a, b) and wind stress (c,d) at the FRF site in Duck, NC (left column) and Martha's Vineyard, MA (right column). a) Monthly averages of buoyancy frequency, N , calculated from daily vertical profiles at the end of the FRF pier (black circles). Line shows seasonal climatology computed from monthly averages. b) Monthly averages and seasonal climatology of N computed from all SWWIM mooring observations at the 7 m site (gray circles and solid line) and 12 m site (black circles and solid line). Monthly averages and climatology of N computed from daily maxima at the 7 m site are also shown (gray triangles and dashed line). c) Wind rose plot for FRF site, showing frequency of occurrence of wind stress magnitude (N/m^2) and direction at FRF site during the months of June-August. The coordinate system has been rotated relative to offshore (x) and upwelling-favorable (y) coordinates shown in Figure 1b. d) As in panel c, for MVCO site and coordinate system shown in Figure 1c.

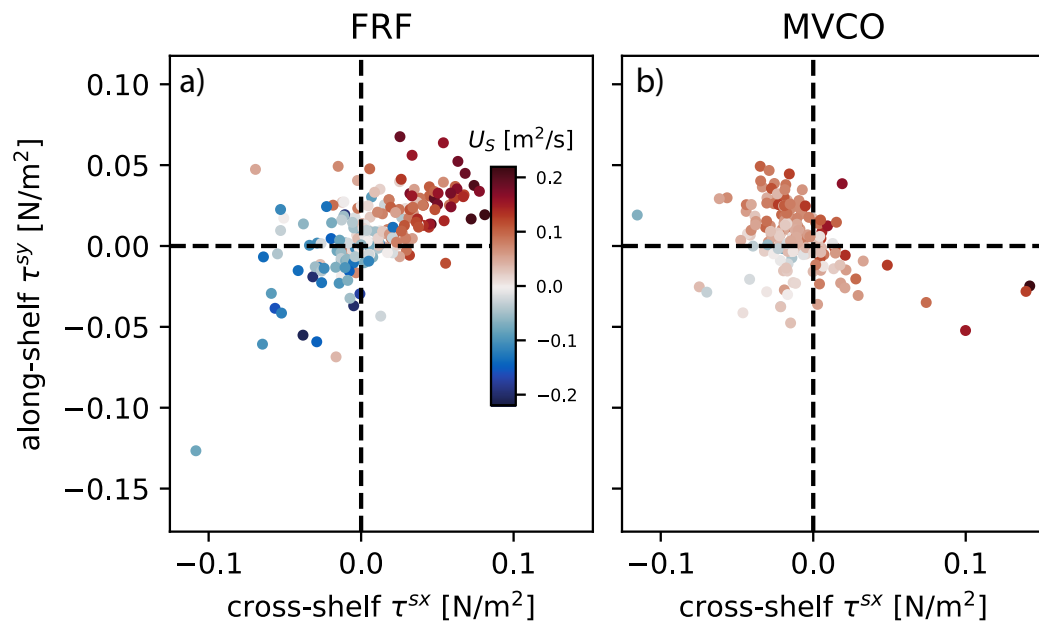


Figure 3: Cross-shelf and along-shelf components of wind stress (τ^{sx}, τ^{sy}) during the months of June-August, with colors indicating surface transport U_s at a) FRF, and b) MVCO. Each point represents a 33-hour average of low-pass filtered data.

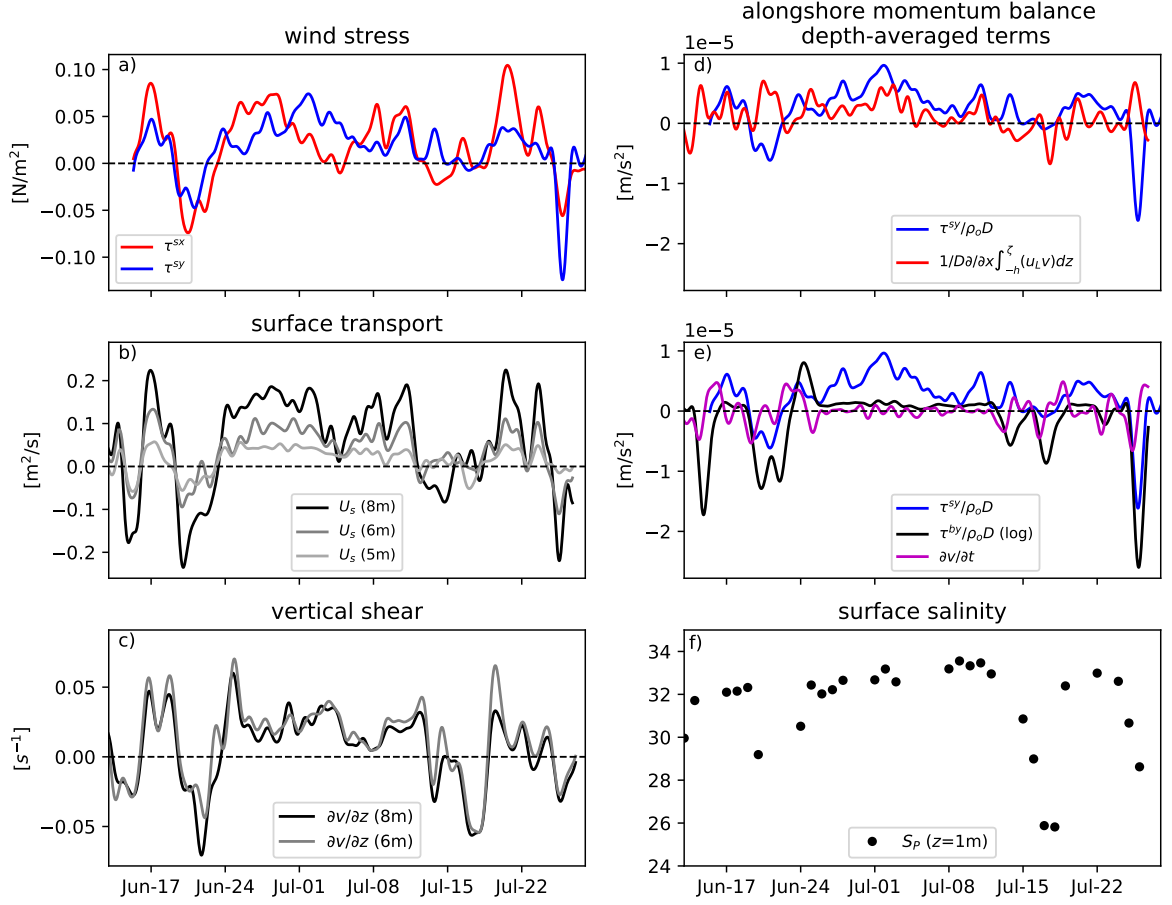


Figure 4: Time series at FRF during the 45-day period 13 June–28 July 2013. a) Cross-shore (red) and alongshore (blue) components of wind stress. b) Cross-shore surface transport, U_s , at the 8 m (black), 6 m (dark gray) and 5 m (light gray) sites. c) Vertical shear in alongshore currents, $\partial v/\partial z$, at the 6 m and 8 m sites. d) Selected terms in the depth-integrated alongshore momentum balance, averaged between the 6 m and 8 m sites: wind stress ($\tau^{sy}/\rho_o D$, blue) and nonlinear advection ($1/D\partial/\partial x \int_{-h}^{\xi} (u_L v) dz$, red). e) Selected terms in the depth-integrated alongshore momentum balance, averaged between the 6 m and 8 m sites: wind stress ($\tau^{sy}/\rho_o D$, blue) and logarithmic bottom stress ($\tau^{by}/\rho_o D$, black). f) Practical salinity, S_P , from CTD casts at a depth of 1 m.

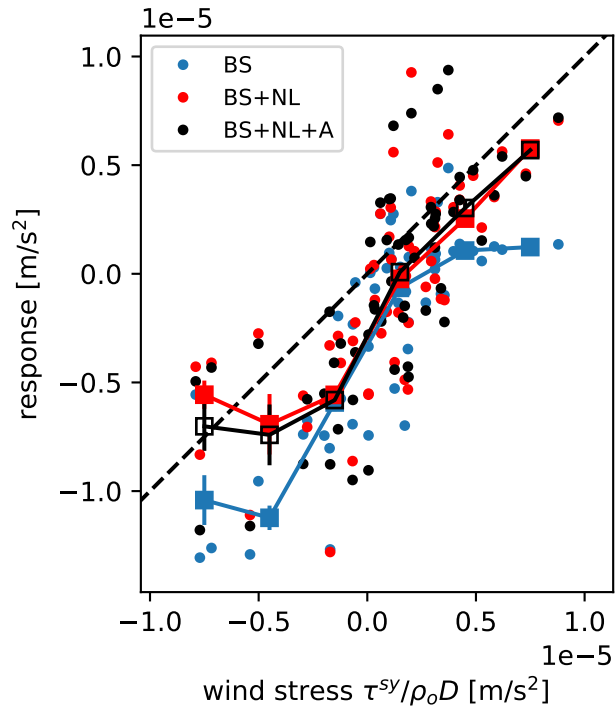


Figure 5: Comparison of wind stress, bottom stress and nonlinear advection terms in the depth-averaged alongshore momentum balance at FRF during June–August. Wind stress term vs. bottom stress (BS) term (blue); wind stress term vs. sum of bottom stress and nonlinear (BS + NL) terms (red); and wind stress term vs. sum of bottom stress, nonlinear and acceleration (BS + NL + A) terms (black). Each circle represents a 33-hour average of low-pass filtered data. Squares are bin averages, with vertical lines showing standard errors.

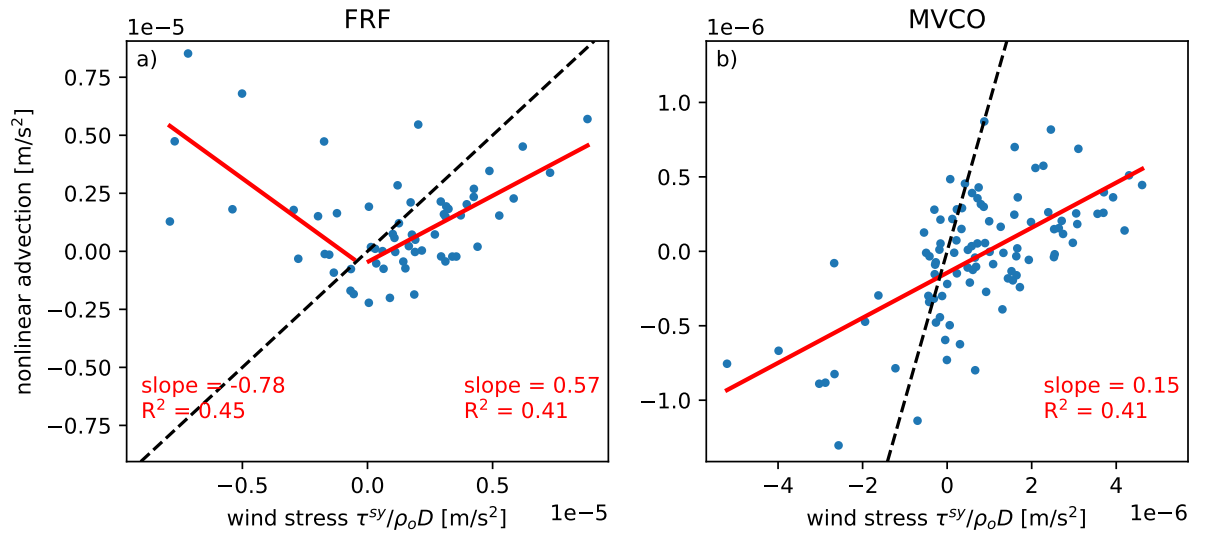


Figure 6: Comparison of wind stress and nonlinear advection terms in the alongshore momentum balance during June–August. a) At FRF over the North Carolina inner shelf. Red lines indicate results of piecewise linear regressions of the 33-hour subsampled values, one regression for positive values of wind stress and another for negative values of wind stress. b) At MVCO over the New England inner shelf. One linear regression is used for both positive and negative values of wind stress. Note difference in scale between panels a and b.

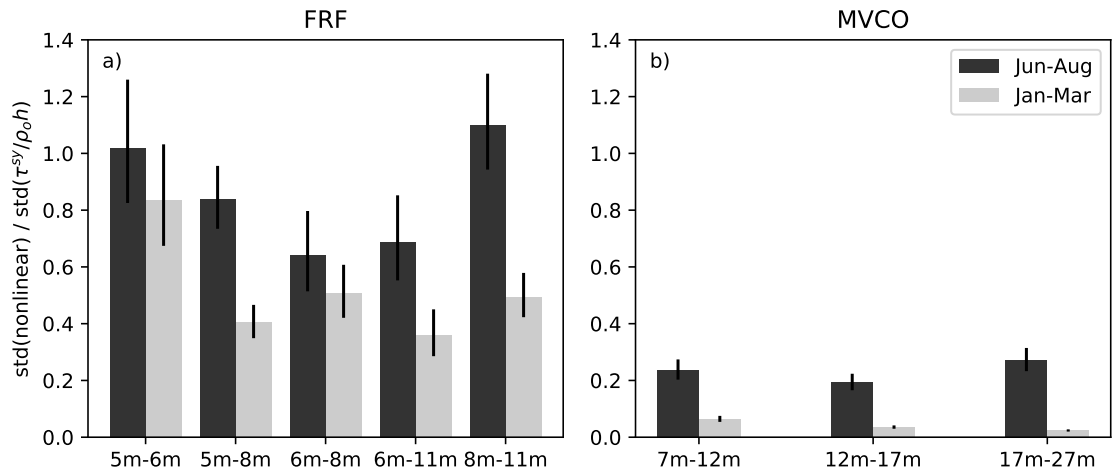


Figure 7: Comparison of variability in the nonlinear and wind stress terms in the alongshore momentum balance. a). Ratio of standard deviations of the nonlinear term and wind stress term at FRF over the North Carolina inner shelf. Black bars show ratios during June–August and gray bars show ratios during January–February. Ratios are shown for five different pairs of sites. Vertical lines indicate 95% confidence intervals. b) As in panel a, for three pairs of sites at MVCO over the New England inner shelf.

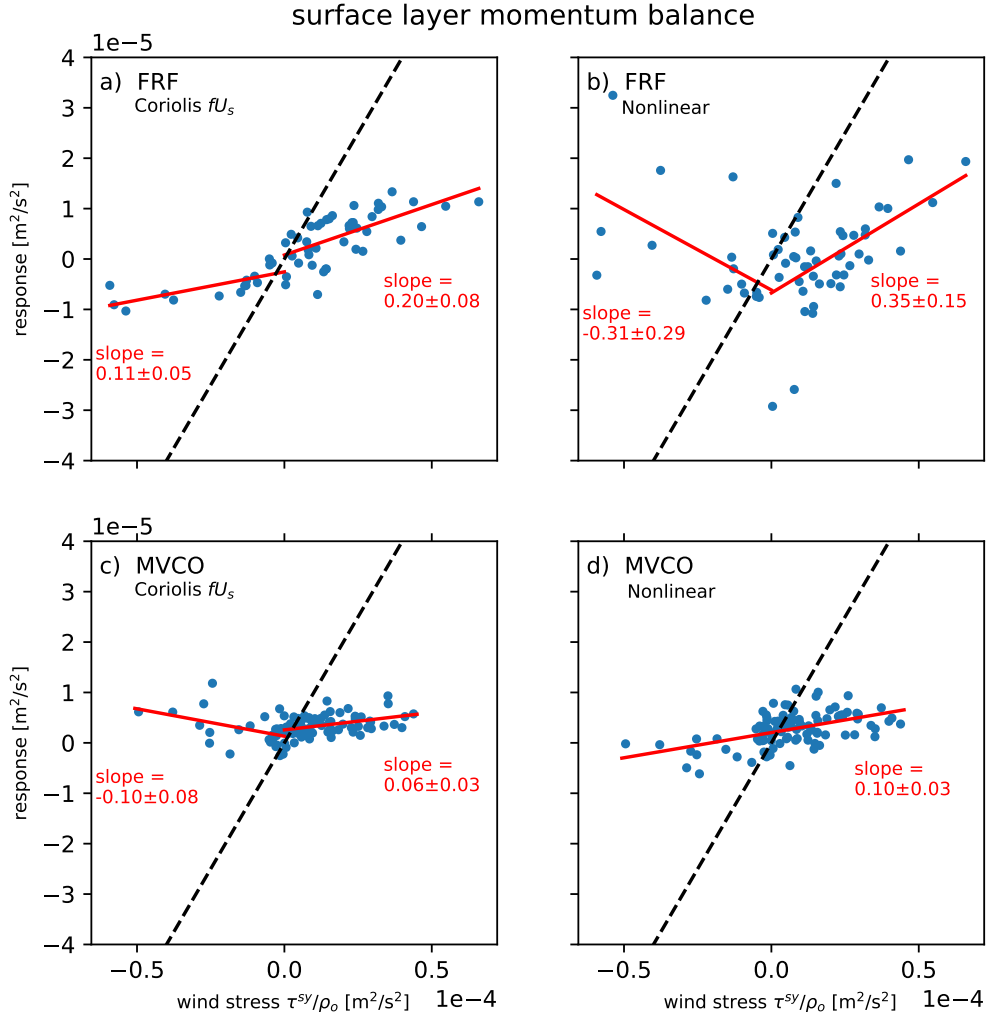


Figure 8: Comparison of wind stress, Coriolis and nonlinear advection terms in the surface layer-integrated alongshore momentum balance at FRF during June–August. a) Wind stress term vs. Coriolis terms at FRF. Each circle indicates a 33-hour average of low-pass filtered data. Lines indicate separate linear regression fits for positive and negative wind stress values. Regression slopes are shown with 95% confidence intervals. b) As in panel a, for wind stress term vs. nonlinear terms at FRF. c) As in panel a, for wind stress term vs. Coriolis term at MVCO. d) As in panel a, for wind stress term vs. nonlinear terms at MVCO, and with one linear regression fit for all data points.

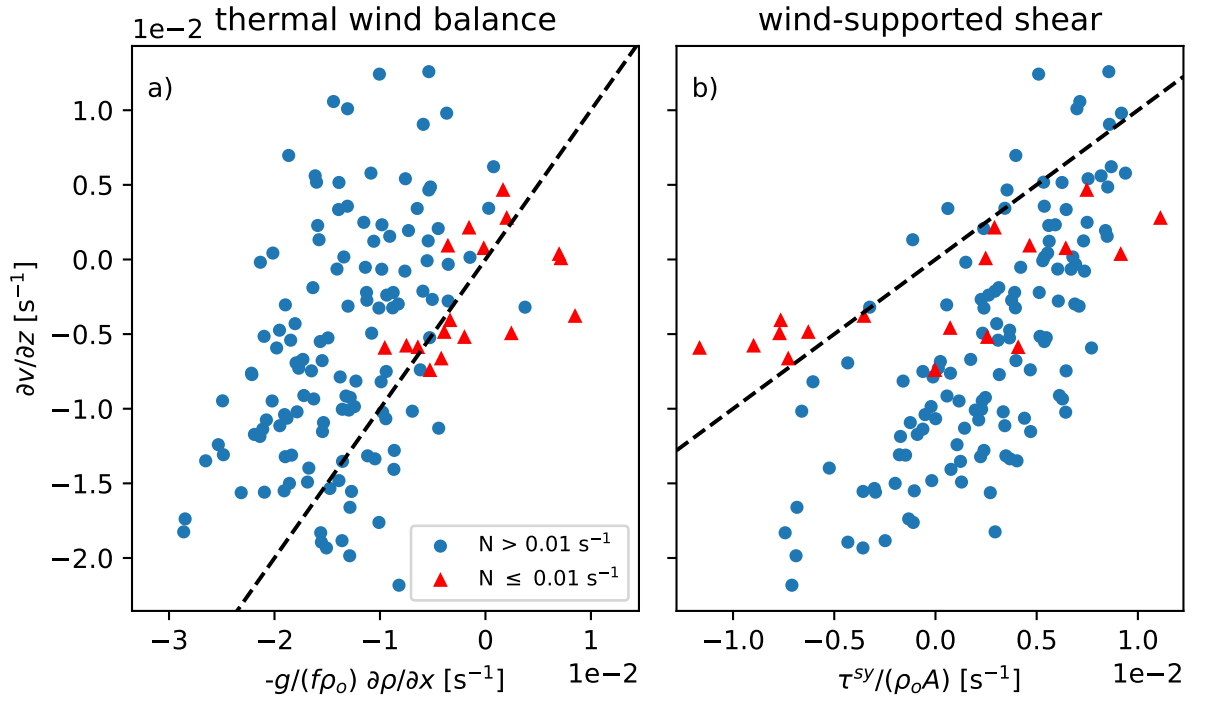


Figure 9: Evaluation of processes governing vertical shear, $\partial v / \partial z$, at MVCO. a) Hypothetical vertical shear associated with thermal wind balance in equation (8). Circles indicate relatively strong stratification, $N > 0.01$. Triangles indicate relatively weak stratification, $N \leq 0.01$. Black dashed line indicates 1:1 relationship. b) Hypothetical vertical shear associated with alongshore wind stress τ^{sy} and eddy viscosity $A = \kappa u_* h / 6$ in equation (9).

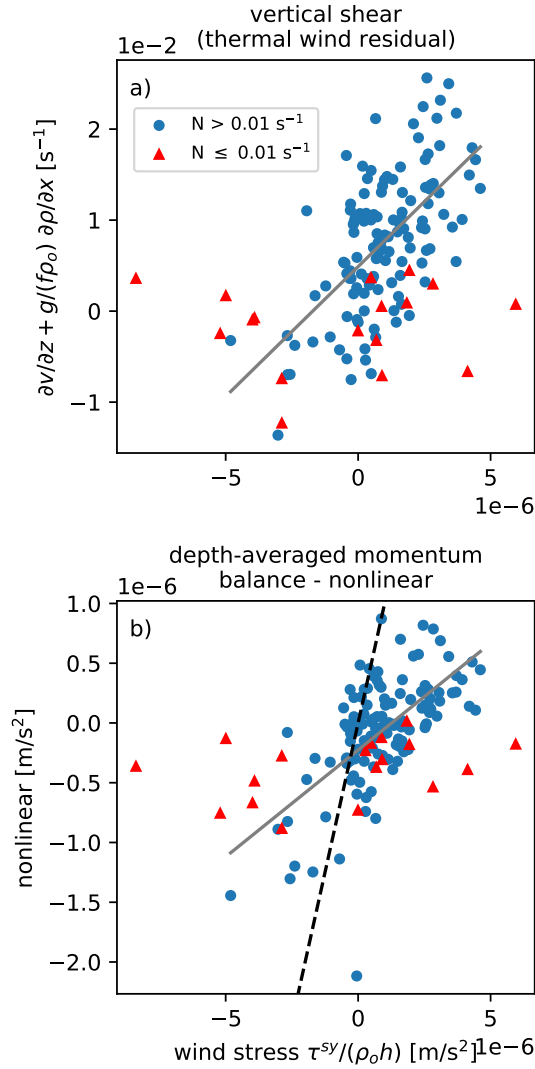


Figure 10: a) Wind stress term $\tau^{sy}/(\rho_0 h)$ vs. the thermal wind balance residual $\partial v/\partial z + g/(f\rho_0)\partial\rho/\partial x$ at MVCO. Circles indicate relatively strong stratification, $N > 0.01$. Triangles indicate relatively weak stratification, $N \leq 0.01$. b) Wind stress and nonlinear advection terms in the depth-averaged momentum balance at MVCO under different levels of stratification.

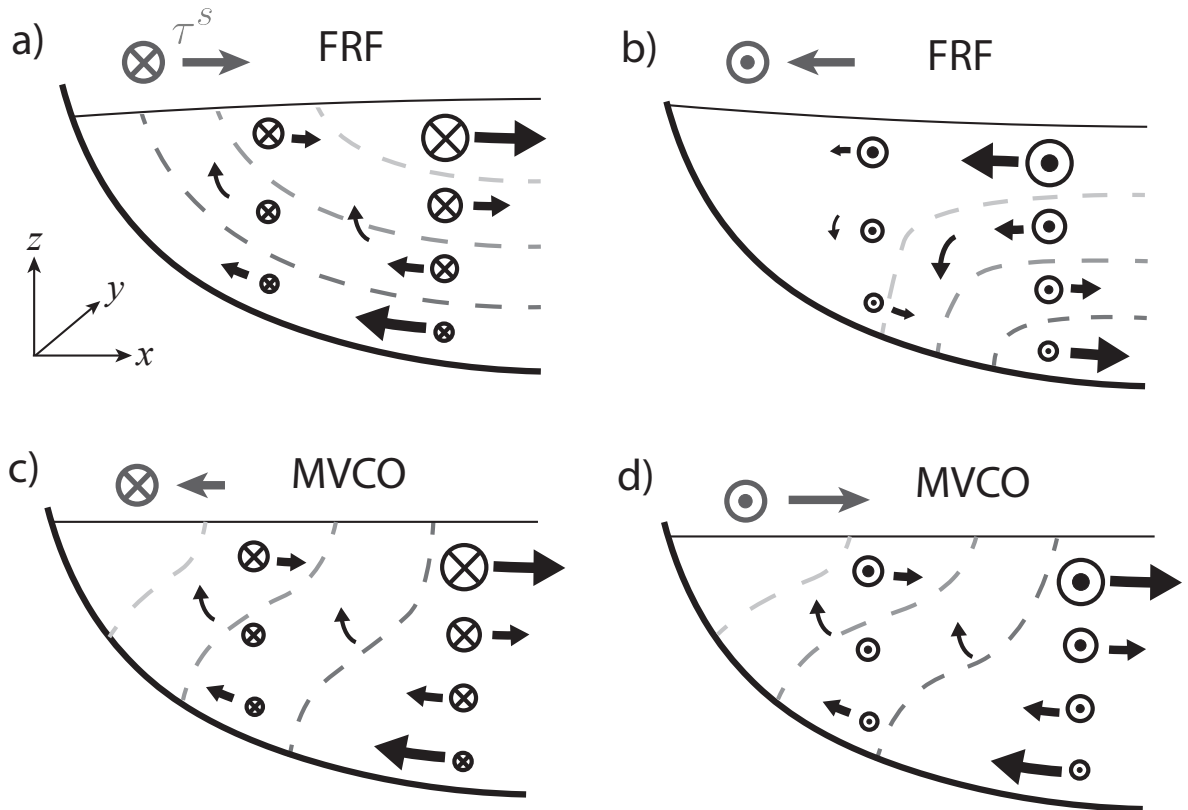


Figure 11: Conceptual models of circulation patterns associated with nonlinear momentum fluxes at different locations and under different forcing conditions. Arrows represent cross-shelf and vertical vector components. Circles represent alongshore vector components (\otimes indicates wind stress or ocean velocity in the positive y direction). Dashed lines indicate isopycnals, where darker shading is relatively dense. a) FRF, upwelling-favorable and offshore wind stress. b) FRF, downwelling-favorable and onshore wind stress. c) MVCO, upwelling-favorable and onshore wind stress. d) MVCO, downwelling-favorable and offshore wind stress.

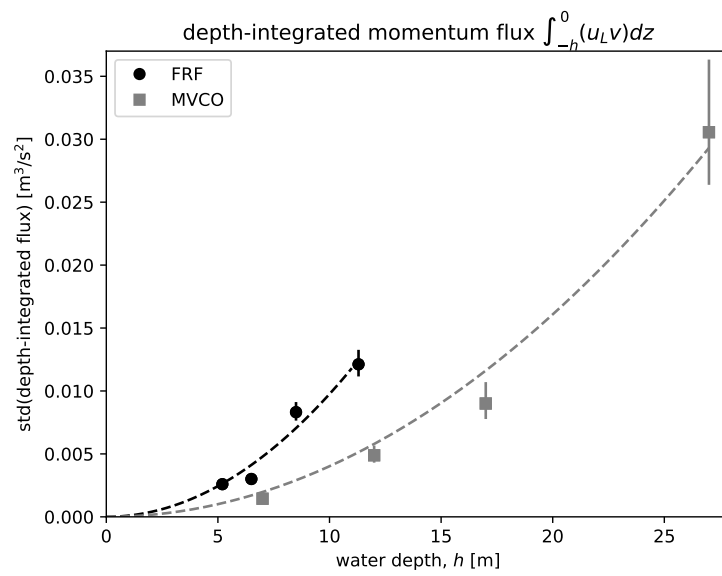


Figure 12: Standard deviations of the depth-integrated nonlinear momentum flux as a function of water depth, for the months of June–August. Black symbols represent estimates from FRF and gray symbols represent estimates from MVCO. Vertical bars indicate 95% confidence intervals. Dashed lines show hypothetical dependence on ah^2 , where a is a constant coefficient obtained from a least squares fit at each location.

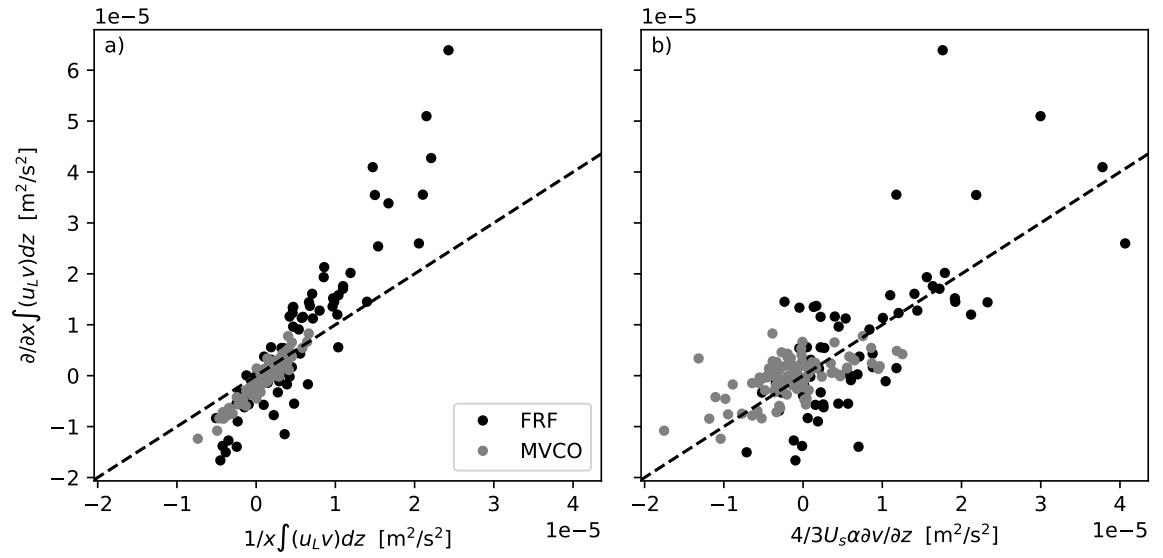


Figure 13: Simplified representations of the nonlinear term in the depth-averaged momentum balance. a) Comparison of the approximation in equation (10) estimated from single deeper mooring (x -axis) vs. full estimate from mooring pairs (y -axis). Black symbols represent estimates from the 6–8m sites at FRF and gray symbols represent estimates from the 7–12m sites at MVCO. Black dashed line represents 1:1 agreement. b) Comparison of the scaling in equation (13) estimated from single deeper mooring (x -axis) vs. full estimate from mooring pairs (y -axis). Symbols as in panel a.